

1 Manuscript for Earth and Planetary Science Letters

2

3 **Title: Evaluating a primary carbonate pathway for manganese enrichments in**  
4 **reducing environments**

5

6 Authors: Chad Wittkop\*(1), Elizabeth D. Swanner (2), Ashley Grengs (1), Nicholas  
7 Lambrecht (2), Mojtaba Fakhraee (3), Amy Myrbo (4), Andrew W. Bray (5), Simon W.  
8 Poulton (5), and Sergei Katsev (3,6)

9

10 \*Corresponding author, [chad.wittkop@mnsu.edu](mailto:chad.wittkop@mnsu.edu), 507-389-6929

11 (1)Department of Chemistry and Geology, Minnesota State University, 241 Ford Hall,  
12 Mankato, MN 56001

13 (2)Department of Geological and Atmospheric Sciences, Iowa State University, 2337  
14 Osborn Drive, Ames, IA, 50011

15 (3)Large Lakes Observatory, University of Minnesota Duluth 2205 East 5th Street,  
16 Duluth, MN 55812

17 (4) St. Croix Watershed Research Station, Science Museum of Minnesota, 16910 152<sup>nd</sup> St  
18 North, Marine on St. Croix, MN 55047 (5) School of Earth and Environment, University  
19 of Leeds, Leeds LS2 9JT, UK

20 (6)Department of Physics, University of Minnesota Duluth, 1049 University Drive,  
21 Duluth, MN 55812

22

23

24 **Abstract**

25

26 Most manganese (Mn) enrichments in the sedimentary rock record are hosted in  
27 carbonate minerals, which are assumed to have formed by diagenetic reduction of  
28 precursor Mn-oxides, and are considered diagnostic of strongly oxidizing conditions.  
29 Here we explore an alternative model where Mn-carbonates form in redox-stratified  
30 water columns linked to calcium carbonate dissolution. In ferruginous Brownie Lake in  
31 Minnesota, USA, we document Mn-carbonates as an HCl-extractable phase present in  
32 sediment traps and in reducing portions of the water column. Mn-carbonate become  
33 supersaturated in the Brownie Lake chemocline where dissolved oxygen concentrations  
34 fall below 5  $\mu\text{M}$ , and Mn-oxide reduction increases the dissolved Mn concentration.  
35 Supersaturation is enhanced when calcite originating from surface waters dissolves in  
36 more acidic waters at the chemocline. In the same zone, sulfate reduction and  
37 microaerobic methane oxidation add dissolved inorganic carbon (DIC) with negative  
38  $\delta^{13}\text{C}$ . These observations demonstrate that sedimentary Mn enrichments may 1) develop  
39 from primary carbonate phases, and 2) can occur in environments with dissolved oxygen  
40 concentrations  $<5 \mu\text{M}$ . Primary Mn-carbonates are likely to originate in environments  
41 with high concentrations of dissolved Mn ( $>200 \mu\text{M}$ ), and where Mn and Fe are  
42 partitioned by S cycling, photoferrotrophy, or microaerophilic Fe-oxidation. A shallow  
43 lysocline enhances Mn-carbonate production by providing additional DIC and nucleation  
44 sites for crystal growth. This carbonate model for Mn-enrichments is expected to be  
45 viable in both euxinic and ferruginous environments, and provides a more nuanced view

46 of the relationships between Mn and carbon cycling, with applications throughout the  
47 rock record.

48

49 **Word count**

50 **6483/6500 (1/14/20)**

51

52 **1. Introduction**

53

54 The strong oxidizing potential ( $E = 1.228$  V) required to form insoluble Mn(IV) oxides  
55 (e.g.  $MnO_2$ , pyrolusite) from reduced and dissolved Mn(II) make sedimentary Mn  
56 enrichments (SMEs) a proxy for the accumulation of oxygen in Earth's early atmosphere  
57 and oceans (Kirschvink et al., 2000; Planavsky et al., 2014). The world's largest SMEs  
58 occur in association with the Great Oxidation Event (GOE, 2.42-2.31 Ga; Gumsley et al.,  
59 2017), but large SMEs persist throughout the geologic record and are broadly correlated  
60 with known fluctuations in Earth's redox balance (Figure 1; Maynard, 2010).

61 Manganese (II)-carbonates are the most common minerals in SMEs, occurring  
62 primarily as rhodochrosite ( $MnCO_3$ ), with lesser amounts of the dolomite group mineral  
63 kutnohorite ( $CaMn[CO_3]_2$ ) and Mn-enriched calcite (Maynard, 2010; Johnson et al.,  
64 2016). These carbonates consistently bear negative carbon isotope signatures (e.g. Tsikos  
65 et al., 2010; Johnson et al., 2013), which are conventionally viewed to indicate diagenetic  
66 reduction (via microbial dissimilatory respiration) of precursor Mn(III/IV)-oxides in  
67 sediment porewater (Calvert and Pederson, 1996).

68 While this diagenetic pathway for Mn-carbonate genesis is favored by most recent  
69 investigators, the implication of precursor Mn-oxides can be controversial. Johnson et al.  
70 (2013) proposed that a 2.42 Ga SME originated from Mn-oxides formed by a  
71 hypothetical Mn-oxidizing photoautotroph. However, these SMEs have alternatively been  
72 viewed as evidence for O<sub>2</sub> accumulation prior to, or at the onset, of the GOE (e.g. Ossa  
73 Ossa et al., 2018), or direct deposition of Mn-carbonates from a stratified water column  
74 (Herndon et al., 2018). Archean SMEs are particularly problematic to explain, but may  
75 represent the emergence of oxygen oases prior to the GOE (e.g. Planavsky et al., 2014),  
76 direct precipitation of Mn-carbonates from seawater (Farquhar et al., 2014), or Mn-  
77 oxidation by a consortia of anoxygenic phototrophs (Daye et al., 2019)

78       Although less commonly invoked in recent interpretations of SMEs, alternative  
79 pathways for Mn-carbonate genesis are feasible in the low-O<sub>2</sub> settings observed in  
80 modern redox-stratified environments (Force and Cannon, 1988). These include  
81 anaerobic metabolisms that generate dissolved inorganic carbon (DIC), increases in pH  
82 that favor carbonate saturation (Rincon-Tomas et al., 2016), or nucleation on Ca-  
83 carbonates (Herndon et al., 2018). Consistent with this view, Mn-carbonates have been  
84 observed in association with reducing conditions in redox-stratified lakes (Nuhfer et al.,  
85 1993; Stevens et al., 2000; Jones et al., 2011).

86       While many lines of evidence converge on the necessity for direct Mn-carbonate  
87 precipitation from redox-stratified water columns, few detailed evaluations of the  
88 processes governing this pathway are available, particularly from ferruginous analogs for  
89 Archean and Proterozoic marine settings (e.g. Crowe et al., 2011). This is exacerbated by

90 the weak carbonate saturation of modern ferruginous lakes (the main analogs for ancient  
91 ferruginous oceans) relative to marine environments.

92 In this work we investigate a recently described ferruginous meromictic lake  
93 (Brownie Lake in Minnesota USA), which hosts both high dissolved Mn concentrations  
94 (up to 130  $\mu$ M) and supersaturation of key carbonate phases, to assess Mn-mineralization  
95 pathways of relevance to anoxic environments across geologic time. We utilize this  
96 setting to evaluate the hypothesis—most recently advanced by Herndon et al. (2018)—  
97 that Mn carbonates may nucleate in the water column of redox stratified lakes. Here we  
98 describe the biogeochemical reactions occurring under ferruginous conditions that drive  
99 Mn-carbonate precipitation, and constrain the oxygen concentrations under which these  
100 processes occur. We then use this framework to assess the potential for anoxic Mn-  
101 carbonate genesis in the rock record, and evaluate the range of processes which may  
102 contribute to the carbonate carbon isotope signatures of these deposits.

103

104

## 105 **2. Study site and methods**

106

107 Brownie Lake (BL) is a small ferruginous lake located in Minnesota, USA. The general  
108 biogeochemistry of the site is described in Lambrecht et al. (2018), and Lambrecht et al.  
109 (2020) presented a detailed study of its methane ( $\text{CH}_4$ ) cycle. Water column profiling,  
110 water sampling and analysis, and geochemical modeling were performed using routine  
111 techniques detailed these publications and in our Supplementary Materials.

112 To assess Mn-phases in the water column, we analyzed particulate material from  
113 water column filtration and sediment traps from intervals representing a transition from  
114 oxic (shallow) to anoxic (deeper) conditions. Particulates were collected on 0.2  $\mu$ M  
115 filters in August 2018 from 4.5, 7, and 10 m depth. Water column sediment traps (at 3.5,  
116 5, and 11 m depth) were deployed from June through October 2018. Surface sediment  
117 samples were also collected in August 2018. Particulate and sediment samples were  
118 processed anaerobically as detailed in Supplementary Materials.

119 Particulate and sediment samples were freeze-dried and Mn was extracted from  
120 50-100 mg of material using 10 mL of 0.5 M HCl for 1 hour, which targets reactive Mn<sup>2+</sup>  
121 and some Fe (Thamdrup et al., 1994; Supplementary Materials). Manganese in the  
122 extractants, as well as total Mn and Al from sediment traps and surface sediments, were  
123 quantified by Atomic Absorption Spectrometry (Thermo Scientific iCE3000 series), with  
124 an RSD of less than 2.1% for all measurements. Sediment trap and surface sediment  
125 samples were further analyzed by X-ray diffraction (XRD), as detailed in Supplementary  
126 Materials.

127 To assess the relationships between carbonate phases and water column  
128 conditions, we developed scenarios in Geochemist's Workbench (GWB) utilizing BL  
129 water chemistry from the depths that displayed the greatest degree of Mn-carbonate  
130 saturation (May 2017 at 6 m; July 2017 at 5.5 and 6 m). At these intervals we considered  
131 a range of inorganic and biological processes that have previously been suggested to  
132 occur at a ferruginous chemocline, including phototrophy, methanotrophy, sulfate (SO<sub>4</sub><sup>2-</sup>)  
133 reduction, and Ca-carbonate dissolution. A full description of our modeling approach can  
134 be found in Supplementary Materials.

135

136

137 **3. Results**

138

139 *3.1 Manganese and carbon cycling in ferruginous Brownie Lake*

140

141 Multi-year water column monitoring of BL demonstrates a stable, redox-stratified,  
142 ferruginous water column, with a chemocline depth (steep concentration gradient of  
143 water column solutes) of 4.5 m and a maximum depth of 14 m (Lambrecht et al., 2018;  
144 Figure 2). Dissolved O<sub>2</sub> concentrations were as high as 402 µM at 1 m depth in April  
145 2017, while values below detection (~3 µM) were reached at depths of 3.5 m in July 2017  
146 and 5 m in October 2015 (Figure 2 a). Concentrations of dissolved Fe, Mn, and SO<sub>4</sub><sup>2-</sup>  
147 follow trends observed in many redox stratified environments (Figure 2 b-d), with  
148 dissolved Mn (interpreted as Mn<sup>2+</sup>) first increasing at the chemocline to a maximum  
149 concentration of 134 µM at 4.5 m in October 2015. Sulfate was present above the  
150 chemocline, with a maximum concentration of 377 µM at 4 m in October 2015 (not  
151 plotted); samples collected in later visits reached a maximum of 122 µM at 2 m in April  
152 2017, but were more typically between 20-40 µM above the chemocline in 2017. Sulfide  
153 concentrations were more variable, with a maximum value of 74 µM recorded at 5 m in  
154 September 2017. Dissolved Fe (interpreted as Fe<sup>2+</sup>) consistently accumulated below the  
155 zones of dissolved Mn maxima and SO<sub>4</sub><sup>2-</sup> drawdown, and rapidly increased below 6 m,  
156 with a maximum value of 1430 µM at 13 m recorded in July 2017.

157 The concentration of DIC ranged from 1.62 mM in surface waters to 14.05 mM at  
158 depth, and generally followed the same pattern of increasing concentration with depth  
159 regardless of the date measured (Figure 2 e). The  $\delta_{13}\text{CDIC}$  ranged from -12.87‰ (5 m  
160 depth, September 2017) to a maximum of -1.97‰ at 12 m depth in May 2017. Regardless  
161 of the date visited, the lowest  $\delta_{13}\text{CDIC}$  values were found near the chemocline, with  
162 highest values at depth, and intermediate values in surface water (Figure 2 f).

163 Dissolved CH<sub>4</sub> concentrations were low near the surface (minimum 2.4 µM at 1 m  
164 depth April 2017) and increased to 1555 µM at depth (12 m, September 2017). Dissolved  
165  $\delta_{13}\text{CCH}_4$  ranged from -64.81‰ (5 m depth, September 2017) to values as high as -21.32‰  
166 (4.5 m in May 2017; Figure 2 h inset). The  $\delta_{13}\text{CCH}_4$  remained between -60 and -64‰  
167 below the chemocline, and increased as dissolved CH<sub>4</sub> concentrations decreased  
168 (Lambrecht et al., 2020).

169

170 *3.2 Brownie Lake pH and mineral solubility*

171

172 Profiles for pH in 2017 (Figure 3 a) demonstrate features consistent with stratification, as  
173 well as seasonal changes. Surface water pH was generally higher than in deep water,  
174 rising as high as 8.85 in May 2017. Lowest pH values were observed below the  
175 chemocline late in the summer, with values as low as 6.26 observed in September 2017.  
176 The pH decrease across the chemocline was smaller in summer months, as demonstrated  
177 by the nearly identical pH profiles in May and July.

178 Surface water samples showed slight calcite supersaturation (Figure 3 b,

179 maximum SI = 0.69 in April 2017; SI = saturation index or Q/K where Q = ion activity

180 product, and  $K =$  given mineral solubility constant), with undersaturation observed in  
181 deeper waters ( $SI = -1.12$  at 9 m depth in September 2017). Below the chemocline the  
182 Mn-carbonate phases pseudokutnahorite (max  $SI = 3.48$  at 6 m depth, July 2017) and  
183 rhodochrosite (max  $SI = 0.46$  at 6 m depth, July 2017) became supersaturated (Figure 3  
184 c). As DIC and  $Fe^{2+}$  accumulated in the deepest waters, siderite ( $FeCO_3$ ) also became  
185 supersaturated, with a maximum  $SI$  of 1.58 observed at 13 m in July 2017 (Figure 3 b). A  
186 closer examination of the key carbonate phases across the 2017 sampling dates (Figure 3  
187 c) suggests that Mn-carbonate saturation varied throughout the summer, while calcite and  
188 siderite remained saturated in surface and deep waters, respectively.

189 Major Fe and Mn oxide phases were supersaturated in surface waters but became  
190 strongly undersaturated in anoxic waters (Lambrecht et al., 2018). The solubility of  
191 phosphate phases in BL is discussed in Supplementary Materials.

192

### 193 *3.3 Particulate and sediment geochemistry*

194

195 Figure 4 displays solid phase Mn data and carbonate mineralogy from three sources in  
196 BL: filtered particulates, sediment traps, and surface sediments. The HCl-extractable Mn  
197 fraction ranged from 862 ppm from the 3.5 m sediment trap, to 189 ppm from a  
198 particulate sample filtered from 10 m depth. The ratio of HCl-extractable Mn to total Mn  
199 in sediment trap and surface sediment samples ranged from 0.070 to 0.085, while total  
200 Mn/Al in these samples ranged from 0.021 to 0.032, with the highest values in both  
201 measures deriving from the 3.5 m sediment trap sample (Figure 4). Sediment trap

202 materials from 5 m displayed more intense XRD peaks for calcite than did surface  
203 sediments.

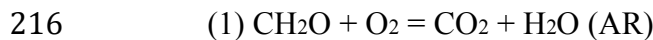
204

205 *3.4 Geochemical modeling*

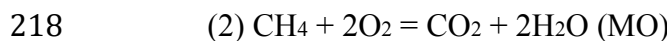
206

207 A process sensitivity analysis and results of simulations for three Mn-carbonate saturated  
208 BL intervals are shown in Figure 5, with model inputs shown in Table 1. After  
209 considering a broader range of potential processes that might influence carbonate  
210 saturation at a ferruginous chemocline (Supplementary Materials), we identified key  
211 relationships in the sensitivity analysis for the July 2017 5.5 m interval (the most strongly  
212 Mn-carbonate supersaturated in our study) that governed the carbonate saturation  
213 behavior of all of our simulations. The first two simulations assessed the role of aerobic  
214 organic carbon respiration (AR) versus aerobic CH<sub>4</sub> oxidation (MO):

215



217



219

220 The key difference between the two processes is the molar ratio of O<sub>2</sub> consumed  
221 to CO<sub>2</sub> produced: 1:1 for AR, and 2:1 for MO. Both scenarios had the same impact on  
222 carbonate saturation. The greater impact of these processes was the removal of O<sub>2</sub>, which  
223 even at the very low concentrations observed in the upper chemocline of BL appears to  
224 inhibit Fe<sup>2+</sup> activity in the model. Complete O<sub>2</sub> removal enhanced Fe<sup>2+</sup> activity and

225 created a subtle boost in siderite saturation (+0.4 Q/K) in both scenarios, with no other  
226 observable differences.

227 Next we considered sulfate reduction (SR), which adds 2 moles of  $\text{HCO}_3^-$  for each  
228 mole of  $\text{SO}_4^{2-}$  consumed.

229

230  $(3) \text{SO}_4^{2-} + 2\text{CH}_2\text{O} = \text{H}_2\text{S} + 2\text{HCO}_3^- \text{ (SR)}$

231

232 Sulfate reduction had a subtle impact on carbonate saturation, with siderite showing the  
233 greatest increase (~0.6 Q/K), followed by rhodochrosite (~0.2 Q/K) then calcite; the  
234 greatest changes occurred in the first two days of the simulation.

235 Next we assessed the addition of calcite at a rate consistent with surface water  
236 calcite saturation from July 2017 (Supplementary Materials). Calcite addition had the  
237 greatest impact on rhodochrosite solubility during the simulation, increasing it by 1.5  
238 Q/K. Calcite solubility had a more subtle response, increasing by only 0.5 Q/K, while  
239 siderite solubility experienced no change in this scenario.

240 The remaining panels in Figure 5 display the impact of the combined processes  
241 (MO, SR, and calcite addition) with varying temperature and pH. Increasing temperature  
242 in the system to 25°C resulted in modest increases in mineral saturation, though the  
243 relative changes are the same for each mineral. Increasing the system pH from 7 to 8.5  
244 resulted in significant increases in mineral saturation, particularly between pH 7.5 and 8.  
245 At the highest pH (8.5), siderite experienced nearly the same increase in Q/K as  
246 rhodochrosite.

247 A final series of scenarios (Figure 5 i-l) considered a solution based on BL  
248 dissolved Fe, Mn, O<sub>2</sub>, and SO<sub>4</sub> values, and adopting modern seawater concentrations for  
249 the remaining ions at pH 8 and a temperature of 25°C. In the first scenario with dissolved  
250 Mn concentration from the BL July 5.5 m interval (Figure 5 i), calcite saturation  
251 increased more than rhodochrosite. However, increasing dissolved Mn concentration in  
252 subsequent seawater scenarios led to significant increases in rhodochrosite Q/K (~+15),  
253 with the maximum observed increase corresponding to a Ca:Mn of 18, which was the  
254 highest observed in BL.

255 Figure 6 shows the impacts of combined SR, MO, and calcite addition on  
256 carbonate mineral saturation from three BL intervals: May 2017 at 6 m, and July 2017 at  
257 5.5 and 6 m, as detailed in Table 1. The results are shown for both mineral precipitation  
258 suppressed (as delta Q/K) and unsuppressed (μmol precipitated) scenarios, as well as the  
259 response in system pH through the course of each simulation.

260 In each suppressed scenario (Figure 6 a-c) rhodochrosite saturation increased the  
261 most, followed by siderite, while calcite saturation increased linearly throughout the  
262 simulation. Siderite saturation displayed a similar pattern in each scenario, with an initial  
263 sharp increase followed by a more gradual climb, and siderite saturation increased nearly  
264 as much as rhodochrosite in the July 2017 6 m scenario (Figure 6 b). In these scenarios  
265 pH gradually increased in each case (Figure 6 d-f)

266 Unsuppressed scenarios demonstrated key differences in the proportions of  
267 minerals produced by these simulations (Figure 6 g-i). One scenario created more calcite  
268 than rhodochrosite, the second created a mixture of the three minerals, and the last

269 precipitated only rhodochrosite. In unsuppressed scenarios, pH changes were generally  
270 more muted (Figure 6 j-i), and system pH was lower overall.

271

272

273 **4. Discussion**

274

275 *4.1 Manganese and carbonate cycling in Brownie Lake*

276

277 Reactive particulate (HCl-extractable) Mn, representative of carbonate-associated Mn,  
278 was present in BL only below the seasonal oxycline (~3.5 m), and represented a  
279 consistent fraction of total anoxic sediment Mn (Figure 4 c.). Coupled with XRD  
280 evidence for calcite dissolution below the BL chemocline (Figure 4 d.), we suggest this  
281 phase most likely consists of calcite crystals precipitated in surface waters, which became  
282 encrusted with Mn-enriched rims during water column settling, resulting in crystals  
283 similar to those previously documented in lake sediments (Stevens et al., 2000; Herndon  
284 et al., 2018).

285 Although we cannot eliminate the possibility that some HCl-extractable Mn in BL  
286 was associated with a non-carbonate phase, such as a poorly crystalline sulfide or  
287 phosphate (see discussion in Supplementary Materials), it is unlikely to represent Mn-  
288 oxides. Mn-oxides are thermodynamically unstable in ferruginous BL as their reduction  
289 is rapidly coupled to the oxidation of Fe(II), sulfide, ammonium and CH<sub>4</sub> (e.g. Jones et  
290 al., 2011), all of which are present in BL waters (Lambrecht et al. 2018; Figure 2).  
291 Furthermore, while HCl-extractable Mn was associated with Mn-oxide phases in

292 ferruginous Lake Matano, this was for samples containing nm-scale oxide filaments  
293 above the chemocline. By contrast, below the Matano chemocline Mn-oxides were  
294 rapidly reduced and replaced by a phase with a XANES spectrum consistent with  
295 rhodochrosite (Jones et al., 2011).

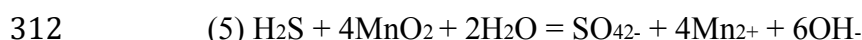
296 The dissolved Mn accumulation in the BL chemocline is among the most  
297 concentrated reported in redox-stratified lakes (up to 134  $\mu$ M), indicating the presence of  
298 a vigorous Mn redox cycle (e.g. Jones et al., 2011; Herndon et al. 2018). Microbial  $Mn^{2+}$   
299 oxidation may contribute to Mn cycling within the BL chemocline, where it is known to  
300 operate efficiently within the  $O_2$  concentration gradients (~3-30  $\mu$ M) observed there  
301 (Clement et al., 2009). Seasonal dynamics of the BL Fe and S cycles may also contribute  
302 to the dissolved Mn pool, as late season sulfide generation by SR drives removal of  
303 dissolved Fe, increasing dissolved Mn:Fe at the top of the chemocline.

304 Water column pH decreased with depth but stabilized at the chemocline before  
305 reaching its lowest values in the deepest waters (Figure 3). This zone of pH stability at  
306 the chemocline was likely driven by a number of processes buffering the overall decline  
307 in pH with depth. For example, Mn-oxide reduction raises pH when coupled to organic  
308 carbon, sulfide, or  $CH_4$  oxidation (Jones et al., 2011; Johnson et al., 2013):

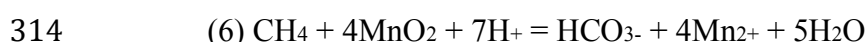
309



311



313



315

316        Of these processes, we consider reactions 4 and 5 most likely to be active at the  
317        BL chemocline, based on the concentrations of species present and the eutrophic nature  
318        of the lake (Lambrecht et al., 2020), which provides a large reservoir of organic carbon to  
319        the system. Similar to reaction 4, iron reduction coupled to organic carbon oxidation is  
320        also capable of decreasing acidity (Walter et al., 2014). While experiments confirm that  
321        reaction 6 can be microbially mediated (Ettwig et al., 2016), organisms putatively  
322        capable of such a reaction were in very low abundance (Lambrecht et al., 2020), and  
323        reaction thermodynamics seem unlikely to support such organisms in BL.

324        Pelagic calcite dissolution, a well-known processes in seasonally stratified lakes  
325        (e.g. Myrbo and Shapley, 2006), may further serve to influence pH and DIC changes at  
326        the chemocline, via:

327

328        (7)  $\text{CaCO}_3 + \text{H}^+ = \text{Ca}^{2+} + \text{HCO}_3^-$

329

330        or by uptake of  $\text{CO}_2$  released through reactions 1 and 2:

331

332        (8)  $\text{CaCO}_3 + \text{CO}_2 + \text{H}_2\text{O} = \text{Ca}^{2+} + 2\text{HCO}_3^-$

333

334        Our solubility calculations (Figure 3), the reduction in intensity of the calcite  
335        XRD peaks between the sediment trap and surface sediments (Figure 4), and the  
336        enrichment in dissolved Ca in the deep waters of BL (Lambrecht et al., 2018), are all  
337        consistent with calcite dissolution occurring near the chemocline.

338 Surface levels of BL carbonate saturation and changes across the chemocline are  
339 similar to those recently documented in euxinic Green Lake, NY (Herndon et al., 2018),  
340 but key differences emerge in the deep ferruginous waters of BL. In Green Lake,  
341 rhodochrosite was only supersaturated in a narrow zone around the chemocline. In BL,  
342 rhodochrosite was supersaturated at and below the chemocline, and siderite became  
343 supersaturated in deep ferruginous waters. This would enable continued Mn-carbonate  
344 crystal growth in deep water, with potential for incorporating Fe into carbonates where  
345 bottom waters are saturated in siderite.

346 Carbonate crystals likely spend sufficient time in Mn-enriched waters to  
347 incorporate significant Mn<sup>2+</sup>. Stokes settling times (at 25° C) for 5  $\mu\text{m}$  crystals through a  
348 non-turbulent, 1.5 m chemocline are on the order of several hours, and increase  
349 exponentially for smaller crystals. Experimental studies (e.g. Pingitore et al., 1988)  
350 suggest Mn<sup>2+</sup> uptake by calcite is favored at slower precipitation rates that would  
351 nonetheless generate significant amounts of Mn-carbonates at these settling velocities  
352 (e.g. 200  $\mu\text{g min}^{-1} \text{m}^{-2}$ ). Hence Mn-carbonate precipitation would be favored in an  
353 environment where  $\mu\text{m}$ -scale crystals settle for several hours or more, and remain in  
354 contact with rhodochrosite supersaturated waters at the sediment-water interface, as is  
355 observed in BL (Figure 3).

356

#### 357 *4.2 Controls on carbonate solubility in Brownie Lake*

358 Our sensitivity analysis demonstrates that calcite addition has the greatest impact on  
359 rhodochrosite saturation in BL (Figure 5). This is likely driven by the relative solubilities  
360 of the two minerals, with more soluble calcite (pK = 8.48 vs. rhodochrosite pK = 10.08,

361 Morse et al., 2007) dissolving at the chemocline and contributing bicarbonate to the  
362 system (eq. 8). The sensitivity of the system to increases in rhodochrosite saturation  
363 appears to be further governed by increasing dissolved Mn concentration (up to 400  $\mu\text{M}$ ),  
364 pH, and temperature. As Fe concentrations increase, such as below the chemocline,  
365 siderite becomes an significant component of the system.

366 Sulfate reduction at the BL chemocline also holds the potential to influence  
367 carbonate saturation. Despite generally low  $\text{SO}_4^{2-}$  concentrations, SR is active in BL  
368 waters, consistent with other ferruginous lakes where vigorous sulfur cycling occurs  
369 (Walter et al., 2014). Because SR generates two mol of  $\text{HCO}_3^-$  for each mol of  $\text{SO}_4^{2-}$ -  
370 reduced (eg. 3), this process drove an initial spike in Fe-Mn carbonate saturation in our  
371 modeled intervals (e.g. Figure 5 c).

372 Unsuppressed scenarios (Figure 6) show that subtle variations in water Mn:Fe and  
373 pH can produce carbonate assemblages with highly variable proportions of Ca-Mn-Fe,  
374 consistent with many ancient examples of Mn enrichments where both Mn-Ca and Mn-Fe  
375 carbonates are reported (Tsikos et al., 2010; Johnson et al., 2016; Planavsky et al. 2018).  
376 Although the assumption of siderite precipitation at 1-fold saturation may be unrealistic  
377 in these scenarios, nucleation on existing crystals may lower the kinetic barriers to  
378 precipitation relative to homogeneous phases (Jiang and Tosca, 2019). Experimental  
379 work previously implicated calcite as a catalyst in Mn-carbonate precipitation. Mucci  
380 (2004) suggested Mn-carbonate minerals could nucleate on small calcite crystals, or  
381 manifest as manganoan rims on calcite if concentrations of  $\text{Ca}^{2+}$  were much greater than  
382  $\text{Mn}^{2+}$ .

383 These scenarios translated well to manganiferous seawater with minor  
384 adjustments. Increasing temperature and pH favored carbonate production (Figure 5 e-h),  
385 but an initial seawater scenario (Figure 5 i) illuminated a challenge to the model:  
386 competition between calcite and rhodochrosite at marine concentrations of Ca. The molar  
387 Ca:Mn of BL water in our sensitivity scenarios derives from a measured value of 25.6,  
388 but scaling to marine Ca increases this ratio to 138 (Table 1). Adjusting the dissolved Mn  
389 concentration of the seawater scenarios to include the highest measured concentration  
390 observed in this study (134  $\mu$ M) led to greater increases in rhodochrosite saturation,  
391 consistent with BL scenarios. Subsequent seawater scenarios with 200  $\mu$ M dissolved Mn,  
392 and a Ca:Mn ratio adjusted to the lowest observed in BL (~18 or a dissolved Mn  
393 concentration of 571  $\mu$ M) generated considerable increases in rhodochrosite saturation  
394 relative to calcite, demonstrating the viability of this mechanism in marine settings.  
395 Although the final scenario had a dissolved Mn concentration over 4-fold larger than we  
396 observed in BL, it is not an unreasonably high concentration for a marine system given  
397 the dissolved Mn concentrations of >400  $\mu$ M reported in the modern Orca Basin (Van  
398 Cappellen et al., 1998).

399

400 *4.3 Dissolved inorganic carbon isotopes in redox-stratified waters*

401

402 Differences in  $\delta^{13}\text{CDIC}$  behavior between euxinic versus ferruginous waters largely derive  
403 from the prominence of the CH<sub>4</sub> cycle in ferruginous systems. Although modern  
404 ferruginous lakes occur in a variety of hydroclimatic settings, data presented here (Figure  
405 2) reinforce the observation that these systems display stratification in  $\delta^{13}\text{CDIC}$ .

406 Ferruginous chemoclines host lower  $\delta_{13}\text{CDIC}$  relative to deep waters that are influenced by  
407 fermentation or methanogenic  $\text{CO}_2$  reduction (Assayag et al., 2008; Crowe et al., 2011;  
408 Lambrecht et al. 2020; Figure 2). Calcite dissolution also holds potential to contribute  
409 heavier DIC to deep waters (Myrbo and Shapley, 2006). In contrast, euxinic lakes also  
410 demonstrate a more common mode of  $\delta_{13}\text{CDIC}$  stratification, wherein waters from the  
411 chemocline and below reflect light  $\delta_{13}\text{CDIC}$  release from AR and SR of organic carbon  
412 (Myrbo and Shapley, 2006; Havig et al., 2017; Figure 7).

413

414 *4.3.1 Impact of methane oxidation on Brownie Lake DIC*

415

416 A pronounced depletion in  $\delta_{13}\text{CDIC}$  at the chemocline and progressive enrichment through  
417 deep anoxic waters reflect active  $\text{CH}_4$  cycling in the BL water column, with oxidation at  
418 the chemocline, and methanogenesis in deep anoxic waters (Lambrecht et al., 2020;  
419 Figure 2 e & f). The increase towards positive  $\delta_{13}\text{C-CH}_4$  consistent with methanotrophy  
420 occurs at the base of the oxycline, at  $\text{O}_2$  concentrations between 4-5  $\mu\text{M}$ . While  $\text{SO}_4^{2-}$   
421 dependent anaerobic oxidation of  $\text{CH}_4$  (AOM) is marginally thermodynamically  
422 permissible in this context, BL 16S rRNA sequencing recovered negligible sequences of  
423 putative AOM archaea (Lambrecht et al., 2020). This is consistent with recent work  
424 demonstrating that aerobic methanotrophy remains favored in ferruginous systems even  
425 at oxygen levels below the detection limit of most sensors ( $\sim 20$  nmol; Oswald et al.,  
426 2016).

427 Both SR and MO are thermodynamically favored in BL (Supplementary  
428 Materials), and capable of influencing  $\delta_{13}\text{CDIC}$ . It is therefore necessary to consider which

429 process may be exerting a greater influence on BL DIC. Employing the reaction-diffusion  
430 approach developed by Crowe et al. (2011), and adopting the vertical eddy diffusivity  
431 value around the chemocline of BL on the order of  $5 \times 10^{-5}$  m<sup>2</sup>/s (Lambrecht et al., 2018),  
432 we calculate that an MO rate of 160  $\mu$ mol/L/day is required to maintain the negative DIC  
433 carbon isotope excursion observed at 4.5 m depth in September 2017. This is within the  
434 range of known lacustrine MO rates, and slightly higher than the maximum rate recently  
435 determined in ferruginous Lake Matano (Sturm et al., 2019). Although dissolved oxygen  
436 concentrations at this interval (~4.7  $\mu$ M) were just above the detection limit of our sonde  
437 (2-3  $\mu$ M), they would be sufficient to maintain aerobic CH<sub>4</sub> oxidation. This rate is also  
438 similar to the upward flux of CH<sub>4</sub> towards the chemocline, as calculated from the CH<sub>4</sub>  
439 concentration profile (90  $\mu$ mol/L/day, assuming oxidation occurs over a 0.5 m interval),  
440 suggesting that the BL carbon isotope excursion could be maintained primarily by MO,  
441 though contributions to the pool of isotopically light DIC from other pathways is further  
442 evaluated below.

443 A mass balance of BL DIC data suggests MO has a stronger influence on the DIC  
444 excursion at the chemocline, with a ratio of ~3:1 MO:SR, consistent with its  
445 thermodynamic favorability (Supplementary Materials). Nitrate- and Fe-Mn-coupled  
446 AOM (Ettwig et al., 2016; Oswald et al., 2016) are intriguing but remote possibilities,  
447 considering such organisms were not significant in BL (Lambrecht et al. 2020).  
448 Concentrations of NO<sub>3</sub><sup>-</sup> observed at Brownie Lake are generally <2  $\mu$ M (Lambrecht et al.,  
449 2018) and are not likely to significantly impact the CH<sub>4</sub> budget. And although it has been  
450 demonstrated in experiments (Ettwig et al., 2016), a clear example of pelagic MO  
451 coupled to Fe/Mn oxide reduction has yet to be produced. Thus, this analysis suggests

452 that aerobic CH<sub>4</sub> oxidation may exert a major influence on  $\delta^{13}\text{CDIC}$  in Brownie Lake,  
453 consistent with the suggestion that methanotrophy is a major influence on  $\delta^{13}\text{CDIC}$  in  
454 ferruginous waters (Crowe et al., 2011).

455

456 *4.3.2 Methane oxidation and carbonate C isotopes*

457

458 The widespread observation of low  $\delta^{13}\text{C}$  in Mn-carbonates is traditionally interpreted as  
459 evidence of diagenetic oxide reduction coupled to organic carbon respiration within  
460 sediments (e.g. Calvert and Pederson, 1996; Planavsky et al., 2018). While this  
461 interpretation is viable in many geological examples, the influence of MO and SR on  
462  $\delta^{13}\text{CDIC}$  in ferruginous lakes demonstrates the potential for embedding signatures of these  
463 processes in primary carbonate minerals.

464 Carbonates derived from CH<sub>4</sub> oxidation have long been recognized (Michaelis et  
465 al., 2002) and are widely described in modern lacustrine and marine environments. In  
466 marine settings, SO<sub>4</sub>-AOM triggers precipitation of carbonates and sulfides (Michaelis et  
467 al., 2002). In completely anoxic and ferruginous settings where SO<sub>42-</sub> is below 10s of  $\mu\text{M}$ ,  
468 benthic archaea have been shown to couple both Fe and Mn-oxide reduction to CH<sub>4</sub>  
469 oxidation (Ettwig et al., 2016), a reaction that similarly favors carbonate precipitation  
470 (Crowe et al., 2011).

471 Aerobic oxidation of CH<sub>4</sub> to CO<sub>2</sub> has a substantially lower redox potential relative  
472 to Mn<sup>2+</sup> oxidation, permitting CH<sub>4</sub> oxidation in suboxic environments where Mn<sup>2+</sup> would  
473 remain reduced (Supplementary Materials). Such a nuanced separation of these processes

474 is possible in a redox-stratified water column, but would be less likely to overlap in  
475 sediments where oxygen would be unlikely to penetrate to a zone of methane production.

476           Earlier interpretations of  $\delta^{13}\text{C}$  from iron formation carbonates suggested greater  
477 variability in the  $\delta^{13}\text{C}$  of marine DIC sources (e.g. Winter and Knauth, 1992), consistent  
478 with the recent suggestion that signatures of hydrothermal DIC may be recorded by some  
479 ancient Fe-carbonates (Jiang and Tosca, 2019). Although the interpretation of primary  
480 versus diagenetic signatures of ancient carbonates remains subject to much debate, it is  
481 clear that a number of primary processes operating in redox-stratified water columns may  
482 generate substantial variability in  $\delta^{13}\text{CDIC}$ .

483

484   *4.4 Mn-carbonates in anoxic environments*

485

486   Recent literature largely assumes that Mn burial in permanently anoxic basins is not  
487 permissible due to the instability of Mn-oxides and high solubility of Mn-sulfides  
488 (Calvert and Pederson, 1996). In the prevailing view, Mn-carbonates form in sediment  
489 porewater after diagenetic reduction of Mn-oxides precipitated from water columns that  
490 are at least episodically oxidized (e.g. Johnson et al., 2013). Our findings, however, are  
491 consistent with work in both ferruginous (Jones et al., 2011) and euxinic lakes (Herndon  
492 et al., 2018), supporting the hypothesis that primary precipitation of Mn-carbonates is  
493 favorable in redox-stratified water columns containing 5  $\mu\text{M}$  of oxygen or less.

494           Observations of Mn-carbonates in sediment traps (Nuhfer et al., 1993), water  
495 column particulates (Jones et al., 2011), and Holocene sediments (Wittkop et al., 2014)  
496 from redox-stratified lakes further support the existence of a primary precipitation

497 pathway. The Mn-carbonate phase documented in Elk Lake, Minnesota was not found in  
498 sediment traps sterilized with formalin (Nuhfer et al., 1993), implicating microbial  
499 processes in its precipitation (Stevens et al., 2000). Consistent with marine examples, the  
500 lacustrine Mn-carbonate overgrowths on calcite crystals documented by Stevens et al.  
501 (2000) corresponded to lighter bulk carbonate  $\delta^{13}\text{C}$  than in intervals without Mn-  
502 carbonates, consistent with a potential role for AR or MO in their origin.

503 This evidence also points to a relatively rapid precipitation of Mn-carbonates  
504 within redox-stratified water columns. Rhodochrosite was identified by XRD in sediment  
505 traps by Nuhfer et al. (1993), and in particulate samples by XANES in Lake Matano  
506 (Jones et al., 2011). Pseudokutnohorite is thermodynamically favored to precipitate  
507 before rhodochrosite (Mucci 2004), but to our knowledge this XRD-amorphous mineral  
508 has not been reported in lacustrine settings, though Stevens et al. (2000) reported  
509 kutnohorite in Holocene sediments.

510

#### 511 *4.5 Application to ancient SMEs*

512

513 In light of the evidence presented here, we advance a primary carbonate model for the  
514 genesis of SMEs (Figure 7 a). The key elements of the carbonate model are, 1) a redox  
515 stratified basin hosting Mn-enriched waters near a redoxcline, 2) Ca-carbonate  
516 precipitation in shallow waters, and 3) a lysocline poised near the basin redoxcline. While  
517 our work demonstrates that this model may be especially viable in ferruginous  
518 environments, it is also consistent with suggestions that Mn-carbonates may represent an  
519 primary precipitate in euxinic settings (Force and Cannon, 1988; Herndon et al., 2018).

520                   Most SMEs occur in shallow water facies (Force and Cannon, 1988), and  
521                   secondary enrichment is precluded in key examples (e.g. Johnson et al., 2013), thus their  
522                   genesis requires the presence of Mn-enriched waters in shallow marine environments,  
523                   and hence a shallow chemocline. Substantial deposits require proximity to hydrothermal  
524                   Mn sources (Maynard, 2010), which may dictate the Mn:Fe of basin waters, but  
525                   additional Fe and Mn segregation may occur at a chemocline as observed in BL. Fe can  
526                   be oxidized by anoxygenic photoferrotrophy in the photic zone (e.g. Lliros et al., 2015),  
527                   or by microaerophilic Fe(II)-oxidizing bacteria (Berg et al., 2019). Both of these  
528                   processes would increase dissolved Mn:Fe. A cryptic sulfur cycle may similarly proceed  
529                   under weakly oxidizing conditions (e.g. Walter et al., 2014), leading to an increase in  
530                   Mn:Fe via Fe-sulfide precipitation (Force and Cannon, 1988).

531                   In contrast to the episodic mixing observed in seasonally-stratified lakes, a more  
532                   stable marine environment would offer the advantage of maintaining the redox  
533                   relationships observed in BL for longer periods of time, enhancing the potential for large-  
534                   scale Mn mineralization. Basin upwelling events may introduce Mn-enriched waters to  
535                   depositional sites, but many SMEs are also linked to marine transgressions (Roy, 2006).  
536                   A transgression could lead to migration of a chemocline over previously deposited Ca-  
537                   carbonates, where Mn-enriched waters would have the opportunity to act as a  
538                   “mineralizing fluid” on surface sediments (Force and Cannon, 1988). Changes in sea  
539                   level may also lead to interbedding of primary carbonates alongside Mn-oxides, which  
540                   could later be diagenetically reduced, accounting for the complex mineral associations  
541                   observed in major Mn enrichments (e.g. Johnson et al., 2016). Independent of eustatic sea

542 level, the chemocline may shift position in response to the relative supply of oxidants  
543 versus reductants in seawater (e.g. Lantink et al. 2018).

544 Capture of Mn by carbonate phases may preclude large-scale oxide precipitation  
545 if the rate of carbonate capture and burial equals or exceeds the rate of Mn supply to the  
546 basin. In contrast, a large Mn-oxide deposit would indicate a rate of Mn upwelling and  
547 oxidation exceeding the rate of capture by carbonates, or a transition to an environment  
548 unfavorable for carbonate production or preservation.

549

550 *4.5.3 The carbonate pathway in Precambrian SMEs*

551

552 Sharp facies gradients between Ca-carbonates and ferruginous or manganiferous  
553 sediments are present in many examples SMEs occurring both before and after the GOE  
554 (e.g. Johnson et al., 2013; Lantink et al., 2018; Ossa Ossa et al., 2018b), implying the  
555 presence of a basin lysocline. The lysocline in small temperate lakes such as BL is driven  
556 primarily by temperature and rates of OM remineralization (e.g. Myrbo and Shapley,  
557 2006). In ancient ferruginous basins, a shallow lysocline may have been further supported  
558 by the presence of metal-enriched hydrothermal waters with a lower pH relative to  
559 surface waters.

560 Recent estimates of dissolved O<sub>2</sub> concentrations derived from Archean SMEs are  
561 higher than the 3-4 μM we considered in our BL simulations, but are generally consistent  
562 with the 3-30 μM range we observe in manganiferous BL waters. The concentrations of  
563 dissolved O<sub>2</sub> represented by Archean SME may have locally exceeded 10 μM (Ossa Ossa

564 et al., 2018), within a range that could support rapid microbial Mn<sup>2+</sup> oxidation and further  
565 concentrate dissolved Mn at a local chemocline (Clement et al., 2009).

566       Although Mn-oxides may be generated in some low-O<sub>2</sub> settings (e.g. Daye et al.  
567 2019), the relationships between O<sub>2</sub> and manganiferous waters in BL imply that efficient  
568 Mn-oxide burial would require O<sub>2</sub> concentrations at the sediment water interface to  
569 remain significantly above 5 μM. We observed O<sub>2</sub> concentrations ranging between ~5-50  
570 μM at the top of the BL chemocline where tens of μM of dissolved Mn began to  
571 accumulate, indicating Mn-oxide reduction was occurring in these waters. Hence Mn  
572 would remain dissolved in environments where O<sub>2</sub> may be present at <5μM—  
573 concentrations that could nonetheless support Fe<sup>2+</sup> and CH<sub>4</sub> oxidation. Here a carbonate  
574 burial pathway for Mn<sup>2+</sup> would remain viable, with the production of various Mn-  
575 minerals dependent on reaction kinetics and the stability of redox gradients.

576       These interpretations are consistent with Fe-isotope evidence from the Hotazel  
577 Formation of the Transvaal Supergroup, deposited near the onset of the GOE. Hotazel  
578 records suggest SME genesis from a redox-stratified basin possessing a large reservoir of  
579 dissolved Fe, and evolving Fe-Mn ratios (Lantink et al. 2018). A primary carbonate  
580 model also accounts for the co-occurrence of Mn(II-III) and Fe(III) phases in Mn-  
581 enrichments interpreted to represent a limited role for diagenetic reduction in the genesis  
582 of Hotazel SMEs (Tsikos et al., 2010).

583       Manganese enrichments in deep water facies of the Proterozoic Animikie Basin  
584 were recently interpreted as evidence of complete water column oxidation (Planavsky et  
585 al. 2018), who invoked a Baltic Sea analog (e.g. Hausler et al., 2018). While the Baltic  
586 Sea SMEs are consistent with deep water oxygenation and genesis from Mn-oxide

587 precursors, they also occur in an environment of very low Fe:Mn, which is not consistent  
588 with the high Fe:Mn of the manganosiderite phases preserved in the Animikie examples  
589 (Planavsky et al, 2018). A primary carbonate genesis of the Animikie examples followed  
590 by continued Fe-carbonate growth on the seafloor (e.g. Figure 7 a.) is more consistent  
591 with both previous work on the Animikie Basin (Poulton et al., 2010), and examples of  
592 highly Mn-enriched Fe-carbonates preserved in ferruginous Holocene sediments  
593 (Wittkop et al., 2014).

594 Although Mo isotope depletions are frequently interpreted as indicators of Mn-  
595 oxide burial (e.g. Planavsky et al., 2018), they may also occur at a euxinic chemocline in  
596 association with changes in Mo-S speciation (Neubert et al., 2008). The co-occurrence of  
597 pyrite with Proterozoic SMEs (Johnson et al., 2013; Planavsky et al., 2018) supports this  
598 view, and opens the possibility that some Precambrian SMEs contain records of cryptic S  
599 cycling as opposed to complete water column oxidation.

600

#### 601 *4.5.4 The carbonate pathway in Phanerozoic SMEs*

602

603 Manganese enrichments from the Neoproterozoic and younger are generally consistent  
604 with more diverse mineralization pathways relative to older examples (Maynard, 2010).  
605 Phanerozoic SMEs are frequently associated with black shales, whose sulfides represent  
606 an effective Fe-sink, allowing for accumulation of dissolved Mn in the water column  
607 (Force and Cannon, 1988). These younger SMEs may remain associated with large-scale  
608 changes in marine redox balance, including ocean anoxic events, and the occurrence of  
609 marine red-beds, which have recently been interpreted as evidence for transient

610 ferruginous episodes in the Phanerozoic (Figure 1; Song et al., 2017). Localized tectonic  
611 influences may overprint this global signal, which is the likely case for the Oligocene  
612 deposits associated with the Black Sea (Force and Cannon, 1988).

613 The Jurassic Molgano deposit of Mexico is the largest Phanerozoic SME,  
614 occurring at the base of a Ca-carbonate facies (Okita, 1992), where it is tellingly not  
615 associated with primary oxides (Force and Cannon, 1988). Instead, detailed mapping of  
616 Mn-phases in Molgano samples suggests manganoan calcite may have represented the  
617 earliest precipitate (Johnson et al., 2016). Other Phanerozoic examples including the  
618 Oligocene Nikopol deposit of Ukraine and Cretaceous Groote Eylandt deposit of  
619 Australia contain Mn-carbonates associated with primary oxides. This co-occurrence of  
620 adjacent oxide and carbonate SMEs within the same sedimentary basin likely represents  
621 the preservation of a water column redox boundary (Force and Cannon, 1988). Careful  
622 re-assessment of such Phanerozoic SMEs utilizing new paleoredox tools is likely to  
623 provide insight into their relationships with global versus localized drivers of their  
624 genesis.

625

626

627 **5. Conclusions**

628

629 We document the production and burial of an HCl-extractable particulate Mn phase,  
630 interpreted as a Ca-Mn-carbonate, from a ferruginous Brownie Lake. Geochemical  
631 models of carbonate production in the lake suggest introduction of calcite to Mn-rich  
632 waters at the chemocline triggers substantial increases in rhodochrosite saturation. These

633 models translate to ferruginous marine conditions, implying a significantly less oxidizing  
634 environment is required to develop carbonate-hosted sedimentary Mn enrichments than  
635 previously recognized. Specifically, our findings suggest primary Mn-carbonates may  
636 originate from waters containing 5  $\mu\text{M}$  dissolved  $\text{O}_2$  or less, and do not require the burial  
637 of precursor Mn-oxides in sediments.

638 Instead of representing diagenetic organic carbon respiration, the negative carbon  
639 isotope composition commonly observed in Mn-carbonates might also be imparted by  
640 organic carbon remineralization or  $\text{CH}_4$  oxidation occurring in the water column. Hence  
641 some sedimentary Mn enrichments may develop where processes operating in low  $\text{O}_2$   
642 environments including sulfur cycling, microaerophilic Fe-oxidation, or anoxygenic  
643 photosynthesis co-occur with a basin lysocline. This interpretation may reconcile  
644 inconsistencies among paleoredox proxies in environments where Mn-enriched sediments  
645 are encountered.

646

647

#### 648 **Acknowledgements**

649 We thank Andrey Bekker, Louis Derry, Frantz Ossa Ossa, and an anonymous reviewer  
650 for suggestions that significantly improved this contribution. J. Barry Maynard  
651 generously shared his compilation of manganese ore data. This study was supported by  
652 an NSF awards (EAR-1660691, EAR-1660761, EAR-1660873) to ES, CW, and SK, and  
653 by NSF-1338322 to AM and others. ES's contribution benefited from support of the Iowa  
654 Space Grant Consortium under NASA Award No. NNX16AL88H. We thank Duncan

655 Widman, Paige Bauer, Raisa Islam, and Gabrielle Ledesma for field and laboratory  
656 assistance.

657

658

659

660

661

662

663

664

665

666

667

668

669

670

671

672

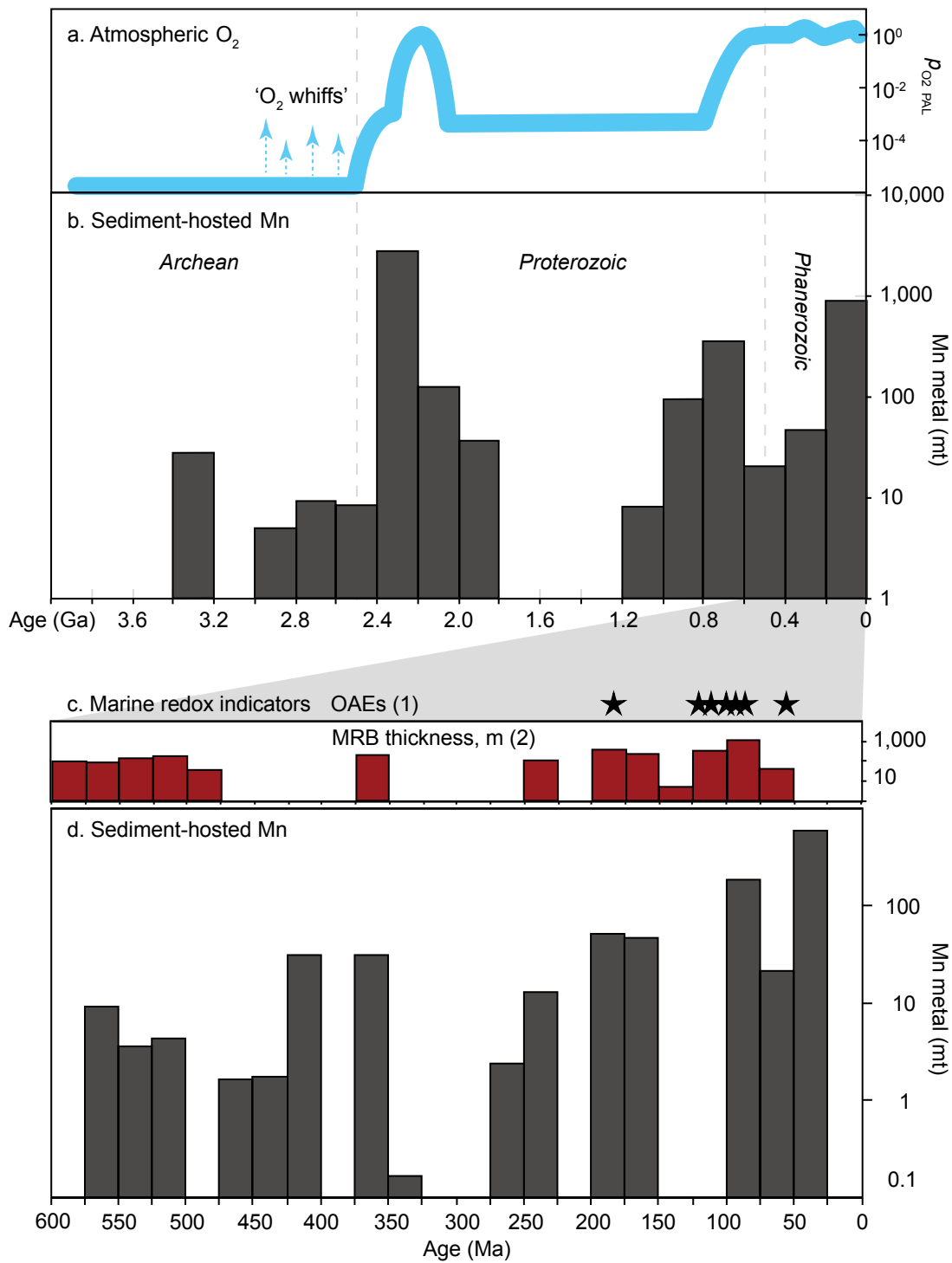
673

674

675

676

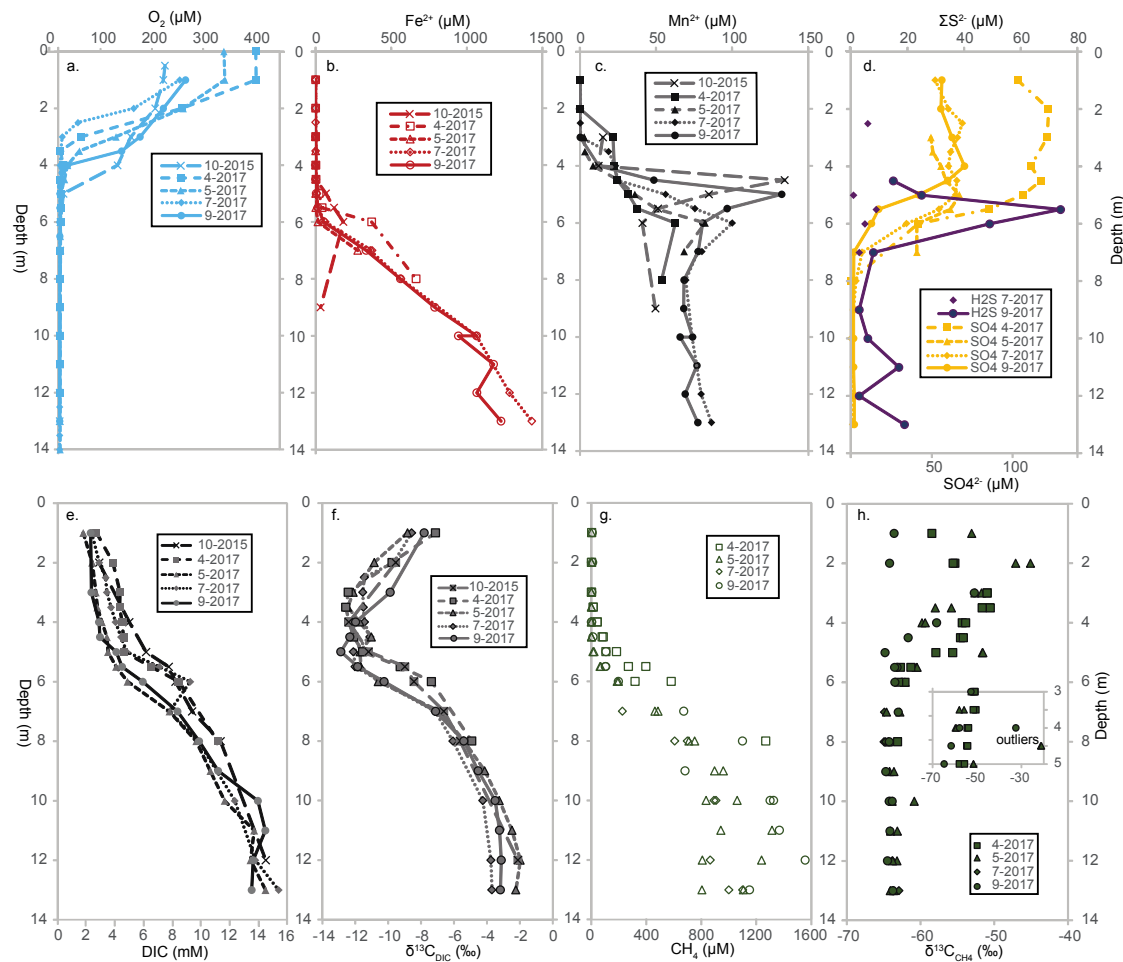
677



680 Figure 1: Sedimentary manganese enrichments (SMEs) through geologic time in  
 681 comparison with redox indicators. Manganese data replotted from Maynard (2010),  
 682 expressed as metric tons Mn metal, including sub-economic and iron-formation hosted  
 683 deposits. a. Atmospheric O<sub>2</sub> from Lyons et al., 2014. b. All SMEs binned in 200 Myr  
 684 increments. c. Post-Neoproterozoic marine redox indicators including ocean anoxic  
 685 events (OAEs; stars) from Jenkyns (2010), and cumulative thickness of marine red beds  
 686 (MRBs), replotted from Song et al. (2017). d. Post-Neoproterozoic SMEs binned in 25  
 687 Myr increments.

688

689

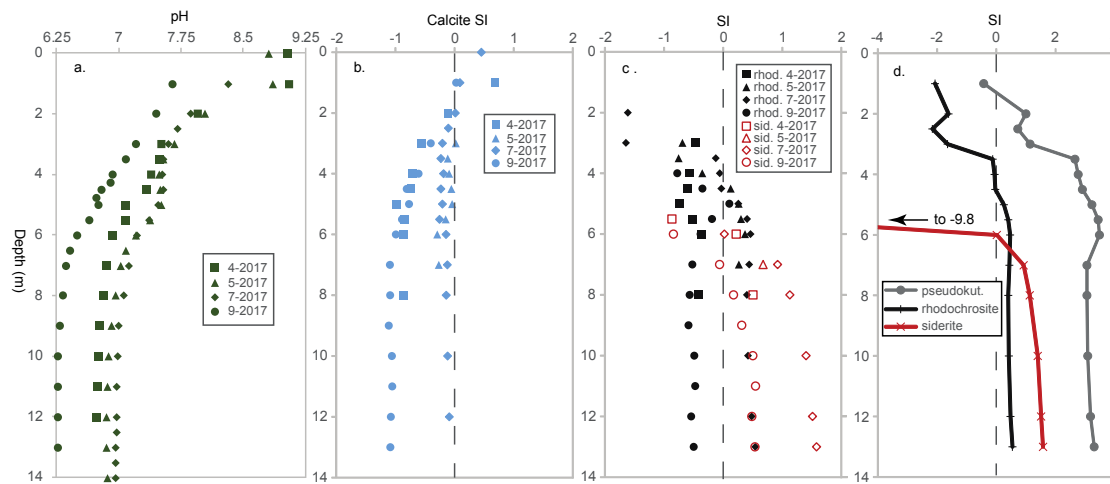


690

691 Figure 2: Brownie Lake 2015-2017 water column profiles of (a) O<sub>2</sub>, (b) dissolved iron  
 692 (Fe<sup>2+</sup>), (c) dissolved manganese (Mn<sup>2+</sup>), (d) SO<sub>4</sub><sup>2-</sup> and total dissolved sulfide ( $\Sigma$  S<sub>2-</sub>), (e)  
 693 dissolved inorganic carbon (DIC), (f) the carbon isotopic composition of DIC, (g)  
 694 dissolved methane (CH<sub>4</sub>), and (h) the carbon isotopic composition of dissolved CH<sub>4</sub>  
 695 (inset shows high values observed near the chemocline). Replotted from Lambrecht et al.  
 696 (2020).

697

698



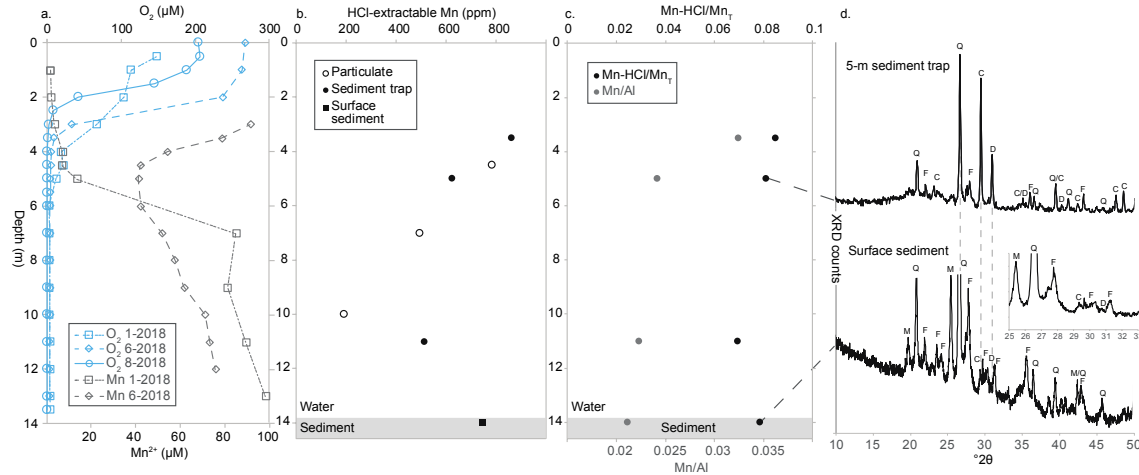
699

700 Figure 3: (a) pH, (b) calcite solubility, and (c) rhodochrosite (rhod.), and siderite (sid.).  
 701 solubility in the Brownie Lake water column in 2017. (d) Detail of July 2017 phases  
 702 including pseudokutnohorite (pseudokut.). Saturation index (SI) =  $\log(IAP/K_{sp})$  where  
 703 IAP is the solution ion activity product and K<sub>sp</sub> is the solubility constant of the given  
 704 mineral.

705

706

707



708

709

710 Figure 4: Brownie Lake particulate and water column data from 2018. (a) Brownie Lake  
 711 water column dissolved  $O_2$  and Mn. (b) Concentrations of HCl-extractable Mn from  
 712 filtered particulates, sediment trap materials, and surface sediments. (c) Sediment trap  
 713 and surface sediment HCl-extractable Mn normalized to total Mn ( $Mn_T$ ), and Mn/Al. (d)  
 714 X-ray diffraction patterns from 5 m sediment trap sample versus surface sediments. Note  
 715 the prominence of the calcite peak in the sediment trap at 5 m relative to surface  
 716 sediments, interpreted as evidence of water column calcite dissolution. XRD peak labels:  
 717 C = calcite, D = dolomite, F = feldspars, M = 2M muscovite, Q = quartz.

718

719

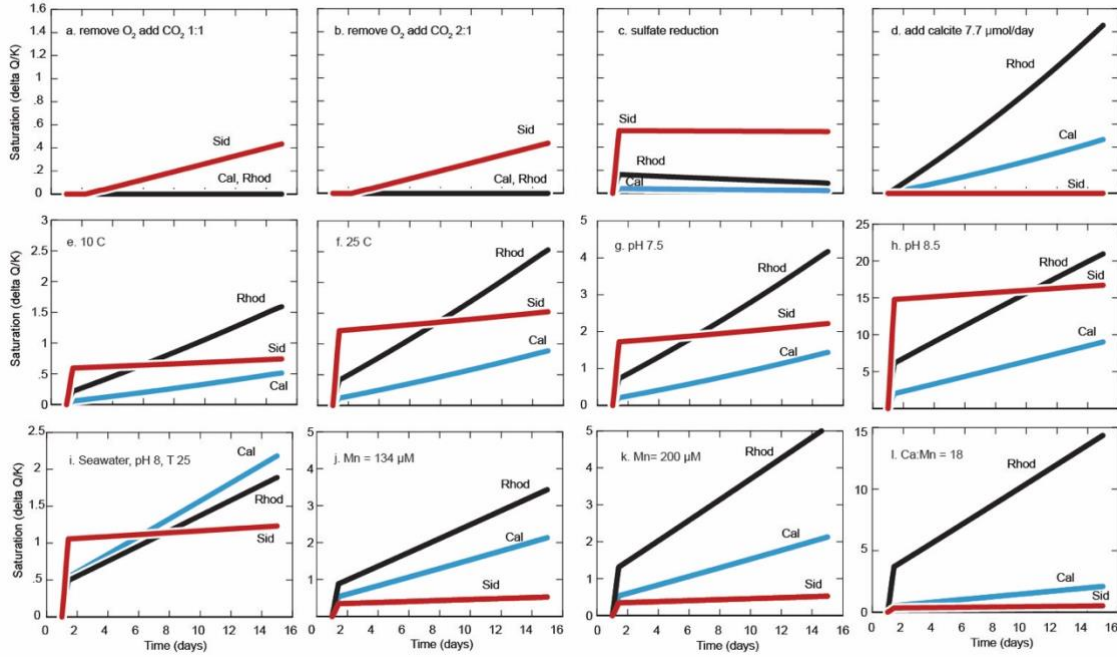
720

721

722

723

724



725

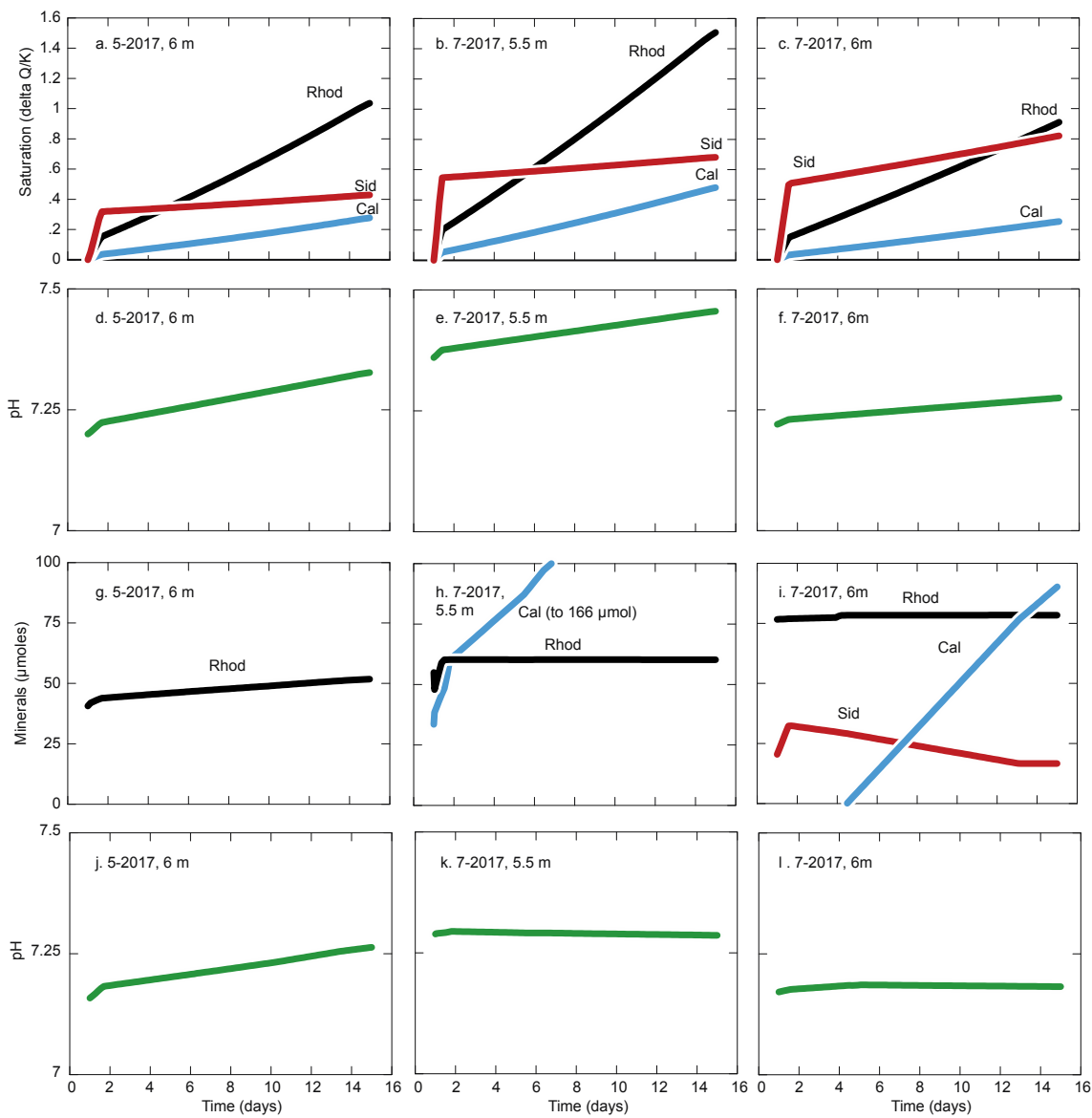
726 Figure 5: Sensitivity of BL carbonate mineral saturation. Cal = calcite (blue), Rhod =  
 727 rhodochrosite (black), and Sid = siderite (red). All changes expressed in terms of delta  
 728 Q/K where Q = IAP and K = given mineral solubility constant. All scenarios are plotted  
 729 in terms of a 15-day simulation and based on BL water chemistry as measured in July  
 730 2017 at 5.5 m (Table 1). See main text for example reactions. (a.) Scenario considering  
 731 aerobic respiration where O<sub>2</sub> and CO<sub>2</sub> are reacted in a 1:1 molar ratio. (b.) Methane  
 732 oxidation scenario where 2 moles of O<sub>2</sub> are consumed for every CO<sub>2</sub> produced. (c.)  
 733 Sulfate reduction scenario. (d.) Addition of calcite at 7  $\mu\text{mol}/\text{day}$  scenario. (e-h.) The  
 734 combination of scenarios b-d. with varying temperature and pH. Note change in scale of  
 735 delta Q/K for g. and h. (i-l.) Scenarios combining b-d. adopting Brownie Lake dissolved  
 736 Fe, Mn, SO<sub>4</sub>, and O<sub>2</sub> concentrations and assuming seawater composition and pH and  
 737 temperature of 25 C. (i.) Seawater with Brownie Lake July 2107 5.5 m concentrations of  
 738 Fe, Mn, SO<sub>4</sub> and O<sub>2</sub>. (j.) Scenario as described in (i.) with dissolved Mn concentration  
 739 increased to 134  $\mu\text{M}$ , the highest observed in our study. (k.) Scenario as described in (i.)

740 with dissolved Mn concentration increased to 200  $\mu\text{M}$ . (l.) Scenario as described in (i.)

741 with Ca:Mn ratio set to 18, the lowest observed in our study.

742

743



744

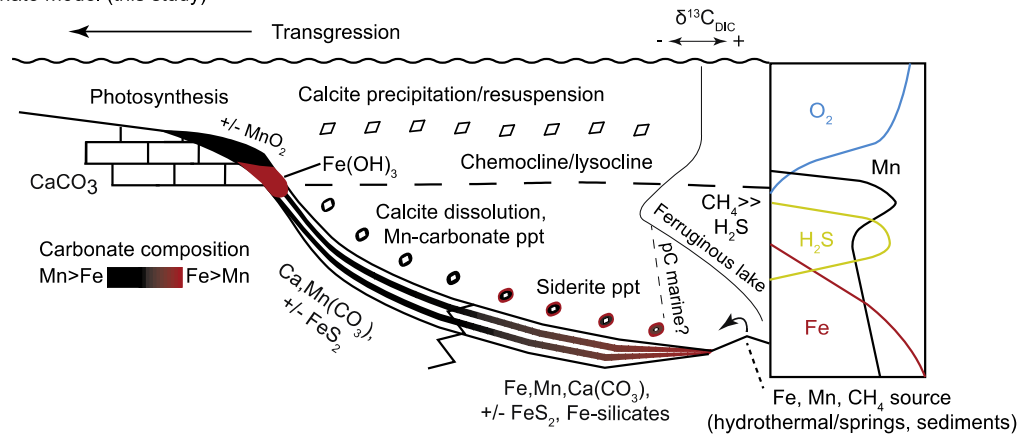
745

746 Figure 6. Combined scenarios for methane oxidation, sulfate reduction, and calcite

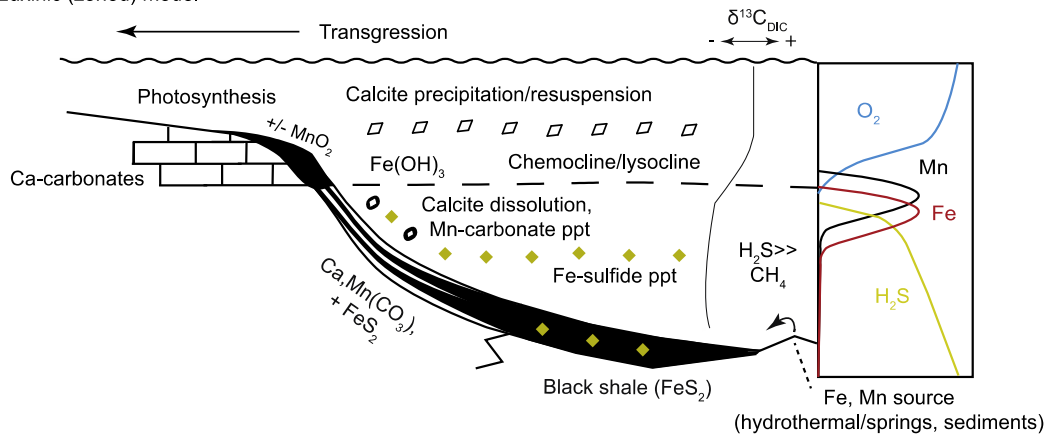
747 addition (i.e. Figure 5 b-d) applied to rhodochrosite-saturated intervals in BL. Mineral

748 abbreviations and Q/K relationships as in Figure 5. Panels a-c with mineral precipitation  
749 suppressed to assess changes in solubility. (a) May 2017 6 m, (b) July 2017 5.5 m, (c)  
750 July 2017 6 m. Panels d-f display pH changes from each of the scenarios above. Panels g-  
751 i display results from unsuppressed simulations where minerals are allowed to precipitate  
752 at Q/K = 1 and accumulate in the system, with mineral concentrations shown in  $\mu$ moles.  
753 Panels j-l display pH evolution of unsuppressed scenarios g-i.  
754

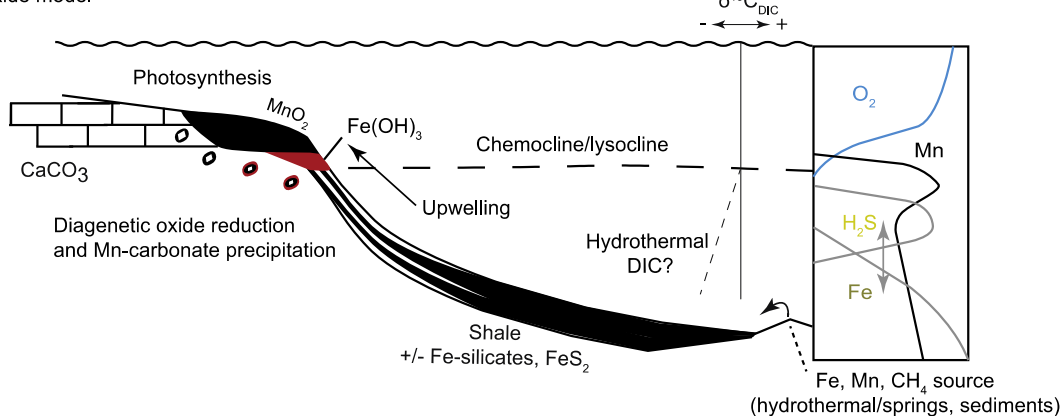
A. Carbonate model (this study)



B. Euxinic (zoned) model



C. Oxide model



755

756

757 Figure 7: Models for the genesis of sediment manganese enrichments (SMEs). Relative  
758 water column composition of  $\delta^{13}\text{C}_{\text{DIC}}$  and concentrations of O<sub>2</sub>, Mn, Fe, and H<sub>2</sub>S (if  
759 applicable) shown to right. Each model assumes the presence of a basin lysocline

760 coincident with a chemocline. Sources of Fe and Mn may include hydrothermal vents,  
761 springs (in lakes), or sediment porewater release. See main text for example reactions. (a)  
762 Carbonate model, based on the ferruginous setting described in this work. Manganese  
763 oxides may not be present if Mn-carbonate genesis rate exceeds rate of supply, and  
764 oxygenic photosynthesis may not have been active in earliest Archean examples. Calcite  
765 introduced to water column via littoral precipitation dissolves as it settles into the  
766 lysocline, where Mn-carbonates nucleate. Fe-rich overgrowths may precipitate (ppt) in  
767 deep waters if siderite saturation is exceeded. Fe-silicates such as greenalite may also co-  
768 precipitate in deep facies of Precambrian oceans (Jiang and Tosca, 2019). The  
769 composition of  $\delta_{13}\text{CDIC}$  is adopted from trends observed in Brownie Lake, but  
770 Precambrian oceans (pC) may not have hosted enriched  $\delta_{13}\text{CDIC}$  in deepest waters.  
771 Transgression is capable of shifting facies relationships to the left, creating contrasting  
772 sediment compositions. (b) Euxinic model, similar to the zoned model of Force and  
773 Cannon (1988) and a mechanism proposed by Herndon et al. (2018). Instead of  
774 carbonates, iron-sulfides dominate in deeper settings, but Mn-carbonates may still  
775 precipitate near the chemocline or if rates of  $\text{CaCO}_3$  accumulation are high throughout  
776 the basin (e.g. Green Lake; Herndon et al., 2018). The  $\delta_{13}\text{CDIC}$  of deep water is shifted  
777 negative due to the predominance of sulfate reduction (Myrbo and Shapley, 2006). (c)  
778 The prevailing oxide model assumes that Mn-carbonates precipitate from a precursor  
779 oxide mineral (e.g. Calvert and Pederson, 1996). A deep water source of dissolved Mn is  
780 still implied. In Precambrian settings ferruginous conditions were likely dominant, but  
781 anoxic basins in the Phanerozoic are often interpreted as euxinic ( $\text{H}_2\text{S}$  rich). Both the

782 carbonate and euxinic model may produce SMEs in suboxic environments, but low  
 783 carbonate saturation or high rates of dissolved Mn upwelling may favor the oxide model.  
 784

*Wittkop et al., in press. Table 1.*

Interval	May 2017 6m		July 2017 5.5m		July 2017 6m		Seawater / July 2017 5.5m	
Species	Conc.	Units	Conc.	Units	Conc.	Units	Conc.	Units
Al <sup>3+</sup>	-	-	0.371	µmol/L	0.408	µmol/L	0.371	µmol/L
B(OH <sub>4</sub> ) <sup>-</sup>	2.868	µmol/L	6.753	µmol/L	6.660	µmol/L	6.753	µmol/L
Ca <sup>2+</sup>	1906	µmol/L	1933	µmol/L	2008	µmol/L	10.28	mmol/kg
Cr <sup>3+</sup>	0.019	µmol/L	0.019	µmol/L	0.038	µmol/L	0.019	µmol/L
Fe <sup>3+</sup>	15.40	µmol/L	11.76	µmol/L	63.57	µmol/L	11.76	µmol/L
K <sup>+</sup>	206.20	µmol/L	192.16	µmol/L	220.52	µmol/L	10.2	mmol/kg
Mg <sup>2+</sup>	720.6	µmol/L	749.3	µmol/L	795.8	µmol/L	52.8	mmol/kg
Mn <sup>2+</sup>	82.15	µmol/L	75.45	µmol/L	99.99	µmol/L	571	µmolar
Na <sup>+</sup>	15046	µmol/L	14720	µmol/L	16666	µmol/L	469	mmol/kg
Cl <sup>-</sup>	20164	µmol/L	16931	µmol/L	18482	µmol/L	546	mmol/kg
Br <sup>-</sup>	33.79	µmol/L	3.755	µmol/L	5.006	µmol/L	0.84	mmol/kg
SO <sub>4</sub> <sup>2-</sup>	40.60	µmol/L	54.13	µmol/L	34.35	µmol/L	54.13	µmol/L
HPO <sub>4</sub> <sup>2-</sup>	0.293	µmol/L	0.592	µmol/L	0.907	µmol/L	0.592	µmol/L
O <sub>2</sub>	4.1	µmol/L	3.13	µmol/L	2.8	µmol/L	3.1	µmol/L
H <sup>+</sup>	7.2	pH	7.36	pH	7.22	pH	8	pH
HCO <sub>3</sub> <sup>-</sup>	4.4	µM	6.5	µM	8.4	µM	1.77	mmol/kg
NO <sub>3</sub> <sup>-</sup>	-	-	-	-	0.1290	µmol/L	-	-
T	7.58	°C	8.33	°C	7.58	°C	25	°C
Ca/Mn	23		26		20		18	
Mn/Fe	5.3		6.4		1.6		49	
Reactant	Rate (µM/day)		Rate (µM/day)		Rate (µM/day)		Rate (µM/day)	
O <sub>2</sub>	-0.27		-0.21		-0.19		-0.21	
CO <sub>2</sub>	0.14		0.10		0.09		0.10	
Calcite	7.70		7.70		7.70		7.70	
SO <sub>4</sub> <sup>2-</sup>	-2.71		-3.61		-2.29		-3.61	
H <sub>2</sub> S	2.71		3.61		2.29		3.61	
HCO <sub>3</sub> <sup>-</sup>	5.41		7.22		4.58		7.22	

785

786

787 Table 1: Inputs and reaction rates for carbonate modeling. Species concentrations (Conc.)  
788 were measured from the BL water column except the seawater scenario, which adopted  
789 values of major dissolved ion concentrations from seawater with the exception of Fe, Mn,  
790 SO<sub>4</sub>, and O<sub>2</sub>. The Mn concentration in the seawater scenario is based on the lowest  
791 observed BL Ca:Mn, with results shown in Figure 5 1. Reaction rates were determined by  
792 dividing the measured concentrations by 15 days, the length of the scenario.

793

794

795

796

797

798

799

800

801

802

803

804

805

806

807

808

809

810 **References Cited (50/50)**

811

812 Assayag, N., Jézéquel, D., Ader, M., Viollier, E., Michard, G., Prévot, F., and Agrinier,  
813 P., 2008. Hydrological budget, carbon sources and biogeochemical processes in Lac  
814 Pavin (France): Constraints from  $\delta^{18}\text{O}$  of water and  $\delta^{13}\text{C}$  of dissolved inorganic carbon:  
815 Applied Geochemistry, v. 23, no. 10, p. 2800-2816.

816

817 Berg, J. S., Jézéquel, D., Duverger, A., Lamy, D., Laberty-Robert, C., & Miot, J. (2019).  
818 Microbial diversity involved in iron and cryptic sulfur cycling in the ferruginous, low-  
819 sulfate waters of Lake Pavin. PLOS ONE, 14(2), e0212787.

820

821 Calvert, S.E., and Pedersen, T.F., 1996. Sedimentary geochemistry of manganese:  
822 Implication for the environment of formation of manganiferous black shales. Economic  
823 Geology v. 91, p. 36-47.

824

825 Clement, B.G., Luther, G.W. III, Tebo, B.M., 2009. Rapid, oxygen-dependent microbial  
826 Mn(II) oxidation kinetics at sub-micromolar oxygen concentrations in the Black Sea  
827 suboxic zone. Geochimica et Cosmochimica Acta, v. 73, p. 1878-1889.

828

829 Crowe, S., Katsev, S., Leslie, K., Sturm, A., Magen, C., Nomosatryo, S., Pack, M.,  
830 Kessler, J., Reeburgh, W., and Roberts, J., 2011, The methane cycle in ferruginous Lake  
831 Matano: Geobiology, v. 9, no. 1, p. 61-78.

832

833 Daye, M., Klepac-Ceraj, V., Pajusalu, M., Rowland, S., Farrell-Sherman, A., Beukes, N.,

834 Tamura, N., Fournier, G., and Bosak, T., 2019. Light-driven anaerobic microbial

835 oxidation of manganese. *Nature*, doi: 10.1038/s41586-019-1804-0.

836

837 Ettwig, K.F., Zhu, B., Speth, D., Keltjens, J.T., Jetten, M.S.M., and Kartal, B., 2016.

838 Archaea catalyze iron-dependent anaerobic oxidation of methane. *Proceedings of the*

839 *National Academy of Sciences*, v. 113, p, 12792-12796.

840

841 Farquhar, J., Zerkle, A.L., and Bekker, A., 2014. 6.4 - Geologic and geochemical

842 constraints on Earth's early atmosphere. *Treatise on Geochemistry*, v. 6, p. 91-138.

843

844 Force, E.R., and Cannon, W.F., 1988. Depositional model for shallow-marine manganese

845 deposits around black shale basins. *Economic Geology*, v. 83, p. 93-117.

846

847 Gumsley, A.P., Chamberlain, K.R., Bleeker, W., Soderlund, U., de Kock, M., Larsson,

848 E.R., and Bekker, A., 2017. Timing and tempo of the Great Oxidation Event. *Proceedings*

849 *of the National Academy of Sciences*, v. 114, p. 1811-1816.

850

851 Hausler, K., Dellwig, O., Schnetger, B., Feldens, P., Leipe, T., Moros, M., Pollehne, F.,

852 Schonke, M., Wegwerth, A., and Arz, H.W., 2018. Massive Mn carbonate formation in

853 the Landsort Deep (Baltic Sea): hydrographic conditions, temporal succession, and Mn

854 budget calculations. *Marine Geology* v. 395, p. 260-270.

855

856 Havig, J.R., Hamilton, T.L., McCormick, M., McClure, B., Sowers, T., Wegter, B., and  
857 Kump, L.R., 2017. Water column and sediment stable carbon isotope biogeochemistry of  
858 permanently redox-stratified Fayetteville Green Lake, New York, USA. Limnology and  
859 Oceanography, v. 63, p, 570-587.

860

861 Herndon, E.M., Havig, J.R., Singer, D.M., McCormick, M.L., and Kump, L.R., 2018.  
862 Manganese and iron geochemistry in sediments underlying the redox-stratified  
863 Fayetteville Green Lake. *Geochimica et Cosmochimica Acta*, v. 231, p. 50-63.

864

865 Jenkyns, H.C., 2010. Geochemistry of ocean anoxic events. *Geochemistry, Geophysics,  
866 Geosystems*, v. 11, doi:10.1029/2009GC002788.

867

868 Jiang, C.Z., and Tosca, N.J., 2019. Fe(II)-carbonate precipitation kinetics and the  
869 chemistry of anoxic ferruginous seawater. *Earth and Planetary Science Letters*, v. 506, p.  
870 231-242.

871

872 Johnson, J.E., Webb, S.M., Thomas, K., Ono, S., Kirschvink, J.L., and Fischer, W.W.,  
873 2013. Manganese-oxidizing photosynthesis before the rise of cyanobacteria. *Proceedings  
874 of the National Academy of Sciences*, v. 110, p. 11238-11243.

875

876 Johnson, J.E., Webb, S.M., Ma, C., and Fischer, W.W., 2016. Manganese mineralogy and  
877 diagenesis in the sedimentary rock record. *Geochimica et Cosmochimica Acta*, v. 173, p.  
878 210-231.

879

880 Jones, C., Crowe, S.A., Sturm, A., Leslie, K.L., MacLean, L.C.W., Katsev, S., Henry, C.,  
881 Fowle, D.A., and Canfield, D.E., 2011. Biogeochemistry of manganese in ferruginous  
882 Lake Matano, Indonesia: Biogeosciences v. 8., p. 2977-2991

883

884 Kirschvink, J.L., Gaidos, E.J., Bertani, E.L., Beukes, N.J., Gutzmer, J., Maepa, L.N., and  
885 Steinberger, R.L., 2000. Paleoproterozoic snowball Earth: Extreme climatic and  
886 geochemical global change and its biological consequences. Proceedings of the National  
887 Academy of Sciences, v. 97, p. 1400-1405.

888

889 Lambrecht, N., Wittkop, C., Katsev, S., Fakhraee, M., and Swanner, E.D. Geochemical  
890 characterization of two ferruginous meromictic lakes in the Upper Midwest, USA, 2018.  
891 Journal of Geophysical Research – Biogeosciences, doi:10.1029/2018JG004587.

892

893 Lambrecht, N., Katsev, S., Wittkop, C., Hall, S.J., Sheik, C.S., Picard, A., Fakhraee, M.,  
894 and Swanner, E.D., 2020. Biogeochemical and physical controls on methane fluxes from  
895 two ferruginous meromictic lakes. Geobiology, v. 18, p. 54-69, doi: 10.1111/gbi.12365.

896

897 Lantink, M.L., Oonk, P.B.H., Floor, G.H., Tsikos, H., and Mason, P.R.D., 2018. Fe  
898 isotopes of a 2.4 Ga hematite-rich IF constrain marine redox conditions around the GOE.  
899 Precambrian Research, v. 305, p. 218-235.

900

901 Lliros, M., Garcia-Armisen, T., Darchambeau, F., Morana, C., Triado-Margarit, X.,

902 Inceoglu, O., Borrego, C.M., Bouillon, S., Servais, P., Borges, A.V., Desey, J-P.,

903 Canfield, D.E., and Crowe, S.A., 2015. Pelagic photoferrotrophy and iron cycling in a

904 modern ferruginous basin. *Scientific Reports*, doi: 10.1038/srep13803.

905

906 Lyons, T.W., Reinhard, C.T., and Planavsky, N.J., 2014. The rise of oxygen in Earth's

907 early ocean and atmosphere: *Nature*, v. 506, p. 307-315.

908

909 Maynard, J.B., 2010. The chemistry of manganese ores through time: A signal of

910 increasing diversity of Earth-surface environments. *Economic Geology*, v. 105, p. 535-

911 552.

912

913 Michaelis, W., Seifert, R., Nauhaus, K., Treude, T., Thiel, V., Blumberg, M., Knittel,

914 K., Gieseke, A., Peterknecht, K., Pape, T., Boetius, A., Amann, R., Jorgensen, B.B.,

915 Widdel, F., Peckman, J., Pimenov, N.V., and Gulin, M.B., 2002. Microbial reefs in the

916 Black Sea fueled by anaerobic oxidation of methane. *Science*, v. 297, p. 1013-1015.

917

918 Morse, J.W., Arvidson, R.S., and Luttge, A., 2007. Calcium carbonate formation and

919 dissolution. *Chemical Reviews*, v. 107, p. 342-381.

920

921 Mucci, A., 2004. The behavior of mixed Ca-Mn carbonates in water and seawater:

922 Controls of manganese concentrations in marine porewaters. *Aquatic Geochemistry*, v.

923 10, p 139-169.

924

925 Myrbo, A., and Shapley, M., 2006, Seasonal water-column dynamics of dissolved  
926 inorganic carbon stable isotopic compositions ( $\delta^{13}\text{CDIC}$ ) in small hardwater lakes in  
927 Minnesota and Montana: *Geochimica et Cosmochimica Acta*, v. 70, no. 11, p. 2699-  
928 2714.

929

930 Neubert, N., Nagler, T.F., and Bottcher, M.E., 2008. Sulfidity controls molybdenum  
931 isotope fractionation into euxinic sediments: evidence from the modern Black Sea.  
932 *Geology* v. 36, p. 775-778.

933

934 Nuhfer, E.B., Anderson, R.Y., Bradbury, J.P., and Dean, W.E., 1993, Modern  
935 sedimentation in Elk Lake, Clearwater County, Minnesota, in Bradbury, J.P., and Dean,  
936 W.E., eds., Elk Lake, Minnesota: Evidence for rapid climate change in the North-Central  
937 United States: Boulder, Colorado, Geological Society of America Special Paper 276, p.  
938 75-96.

939

940 Okita, P.M., 1992. Manganese carbonate mineralization in the Molgano District, Mexico.  
941 *Economic Geology*, v. 87, p. 1345-1366.

942

943 Ossa Ossa, F., Hofmann, A., Wille, M., Spangenberg, J.E., Bekker, A., Poulton, S.W.,  
944 Eickmann, B., and Schoenberg, R., 2018a. Aerobic iron and manganese cycling in a  
945 redox-stratified Mesoarchean epicontinental sea. *Earth and Planetary Science Letters*, v.  
946 500, p. 28-40.

947

948 Ossa Ossa, F., Eickmann, B., Hofmann, A., Planavsky, N.J., Asael, D., Pambo, F., and  
949 Bekker, A., 2018b. Two-step deoxygenation at the end of the Paleoproterozoic  
950 Lomagundi Event. *Earth and Planetary Science Letters*, v. 486, p. 70-83.

951

952 Oswald, K., Jegge, C., Tischer, J., Berg, J., Brand, A., Miracle, M.R., Soria, X., Vicente,  
953 E., Lehmann, M.F., Zopfi, J., and Schubert, C.J., 2016. Methanotrophy under versatile  
954 conditions in the water column of the ferruginous meromictic Lake La Cruz (Spain).  
955 *Frontiers in Microbiology*, v. 7, doi:10.3389/fmicb.2016.01762.

956

957 Pingitore, N.E., Eastman, M.P., Sandige, M., Oden, K., and Freiha, B., 1988. The  
958 coprecipitation of Manganese(II) with calcite: an experimental study. *Marine Chemistry*,  
959 v. 25, p. 107-120.

960

961 Planavsky, N.J., Asael, D., Hofmann, A., Reinhard, C.T., Lalonde, S.V., Knudsen, A.,  
962 Wang, X., Ossa Ossa, F., Pecoits, E., Smith, A.J.B., Beukes, N.J., Bekker, A., Johnson,  
963 T.M., Konhauser, K.O., Lyons, T.W., and Rouxel, O.J., 2014. Evidence for oxygenic  
964 photosynthesis half a billion years before the Great Oxidation Event. *Nature Geoscience*,  
965 v. 7, p. 283-286.

966

967 Planavsky, N.J., Slack, J.F., Cannon, W.F., O'Connell, B., Isson, T.T., Asael, D.,  
968 Jackson, J.C., Hardisty, D.S., Lyons, T.W., and Bekker, A., 2018. Evidence for episodic

969 oxygenation in a weakly redox buffered deep mid-Proterozoic ocean. Chemical  
970 Geology, v. 483, p. 581-594.

971

972 Poulton, S.W., Fralick, P.W., and Canfield, D.E., 2010. Spatial variability in oceanic  
973 redox structure 1.8 billion years ago. *Nature Geoscience*, v. 3, p. 486-490.

974

975 Rincon-Tomas, B., Khonsari, B., Muhlen, D., Wickbold, C., Schafer, N., Hause-Reitner,  
976 D., Hoppert, M., and Reitner, J., 2016. Manganese carbonates as possible biogenic relics  
977 in Archean settings. *International Journal of Astrobiology*, v. 15, p. 219-229.

978

979 Roy, S., 2006. Sedimentary manganese metallogenesis in response to the evolution of the  
980 Earth system. *Earth-Science Reviews*, v. 77, p. 273-305.

981

982 Song, H., Jiang, G., Poulton, S.W., Wignall, P.B., Tong, J., Song, H., An, Z., Chu, D.,  
983 Tian, L., She, Z., and Wang, C., 2017. The onset of widespread marine red beds and the  
984 evolution of ferruginous oceans. *Nature Communications*, doi: 10.1038/s41467-017-  
985 00502-x

986

987 Stevens, L.R., Ito, E., and Olson, D.E.L., 2000. Relationship of Mn-carbonates in varved  
988 lake-sediments to catchment vegetation in Big Watab Lake, MN, USA. *Journal of*  
989 *Paleolimnology*, v. 24, p. 199-211.

990

991 Sturm, A., Fowle, D.A., Jones, C., Leslie, K., Nomosatryo, S., Henry, C., Canfield, D.E.,  
992 and Crowe, S.A., 2019. Rates and pathways of CH<sub>4</sub> oxidation in ferruginous Lake  
993 Matano, Indonesia. *Geobiology*, v. 17, p. 294-307.

994

995 Thamdrump, B., Fossing, H., and Jorgensen, B.B., 1994. Manganese, iron, and sulfur  
996 cycling in a coastal marine sediment, Aarhus Bay, Denmark. *Geochimica et*  
997 *Cosmochimica Acta*, v. 58, p. 5115-5129.

998

999 Tsikos, H., Matthews, A., Erel, Y., and Moore, J.M., 2010. Iron isotopes constrain  
1000 biogeochemical redox cycling of iron and manganese in a Paleoproterozoic stratified  
1001 basin. *Earth and Planetary Science Letters*, v. 298, p. 125-134.

1002

1003 Van Cappellen, P., Viollier, E., Roychoudhury, A., Clark, L., Ingall, E., Lowe, K., and  
1004 Dichristina, T., 1998. Manganese and Iron at the oxic-anoxic transition of a stratified  
1005 marine basin (Orca Basin, Gulf of Mexico). *Environmental Science and Technology*, v.  
1006 32, p. 2931-2939.

1007

1008 Walter, X.A., Picazo, A., Miracle, M.R., Vicente, E., Camacho, A., Aragno, M., and  
1009 Zopfi, J., 2014. Phototrophic Fe(II)-oxidation in the chemocline of a ferruginous  
1010 meromictic lake. *Frontiers in Microbiology*, doi: 10.3389/fmicb.2014.00713.

1011

1012 Winter, B. L., and Knauth, L. P., 1992, Stable isotope geochemistry of cherts and  
1013 carbonates from the 2.0 Ga Gunflint Iron Formation: implications for the depositional

1014 setting, and the effects of diagenesis and metamorphism: Precambrian Research, v. 59,  
1015 no. 3, p. 283-313.

1016

1017 Wittkop, C., Teranes, J., Lubenow, B., and Dean, W.E., 2014, C- and O-stable isotopic  
1018 signatures of methanogenesis, temperature, and water column stratification in Holocene  
1019 siderite varves. Chemical Geology, v. 389, p. 153-166.

1020

1021

1022

1023

1024

1025

1026

1027

1028

1029

1030

1031

1032

1033

1034

1035

1036

1037 **The carbonate pathway for formation of manganese enrichments in reducing**  
1038 **environments**

1039

1040 Authors: Chad Wittkop, Elizabeth D. Swanner, Ashley Grengs, Nicholas Lambrecht,  
1041 Mojtaba Fakhraee, Amy Myrbo, Andrew W. Bray, Simon W. Poulton, and Sergei Katsev

1042

1043 **Supplementary Materials**

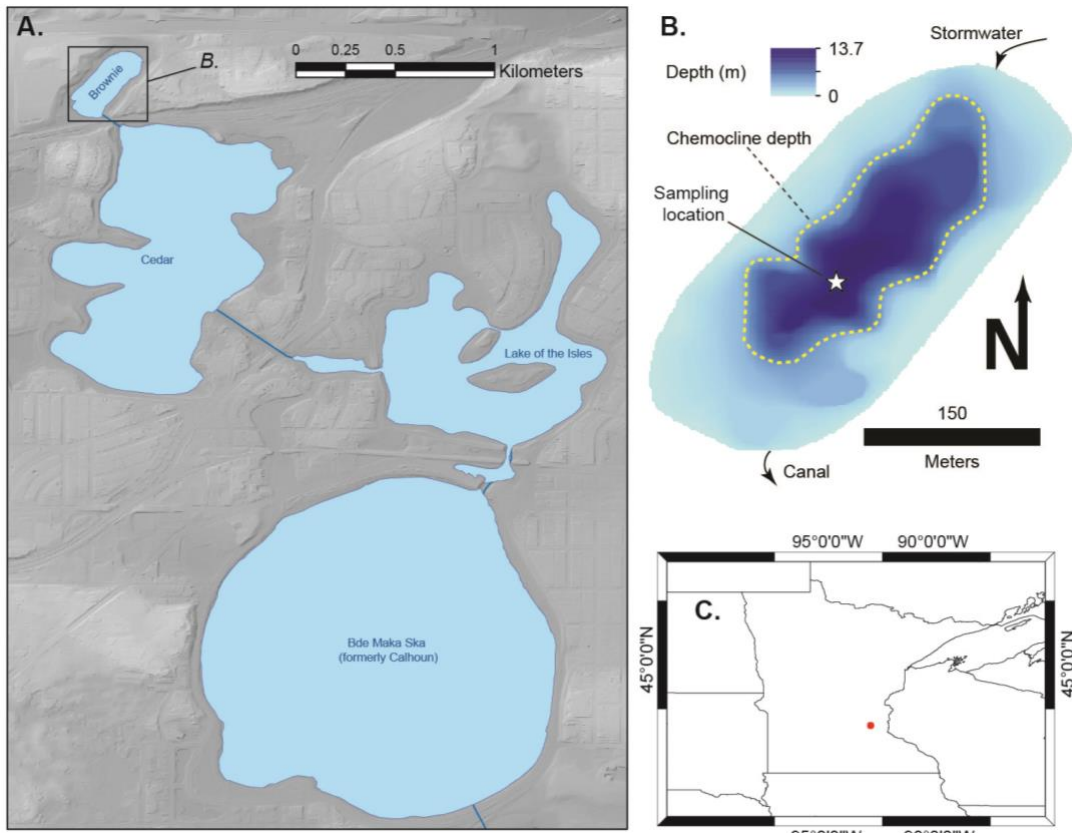
1044

1045 **S1. Study site**

1046

1047 Brownie Lake (BL) is a small ferruginous kettle lake located in Minneapolis, Minnesota  
1048 (N44.9676° W93.3245°; figure S1). Historical and paleolimnologic analysis suggests that  
1049 BL has been meromictic since 1917, when its surface elevation was lowered by  
1050 construction of a canal joining it with adjacent Cedar Lake (Swain, 1984; Tracey et al.,  
1051 1996). Profundal sediments are continuously laminated above this horizon, and  
1052 laminations are annual (Swain, 1984). BL surface area is 4.0 ha (compared to 13.2 ha  
1053 pre-1917), and its max depth is now 14 m (compared to an estimated 17 m). The lake's  
1054 reduced surface area and fetch, and surface elevation low in its basin, have reduced its  
1055 susceptibility to wind entrainment of surface waters and vertical water column mixing.  
1056 An industrial cooling water outlet also contributed to increased concentrations of  
1057 dissolved Fe<sub>2+</sub>, alkalinity, and SiO<sub>2</sub> in the late 20th century (Swain, 1984), and  
1058 contamination from road salt has further increased total salinity and stability of the water  
1059 column (Novonty et al., 2008; Myrbo et al., 2011; Lambrecht et al., 2018). Isolation of  
1060 the cold (7°C) lake bottom waters from atmospheric O<sub>2</sub> resupply, along with a high flux  
1061 of algal and terrestrial organic carbon, have driven evolution to low Eh and pH  
1062 conditions, under which minerals such as iron (hydr)oxides and carbonates may dissolve,  
1063 increasing bottom water density and strengthening stratification. The persistent, stable  
1064 nature of the stratification is particularly evident in repeated monitoring of water column  
1065 conductivity (Lambrecht et al. 2018).

1066



1067  
1068

1069 *Figure S1: A. Location of Brownie Lake relative to the Minneapolis Chain of Lakes. B.*  
1070 *Brownie Lake bathymetry showing sampling location and approximate area of anoxic*  
1071 *zone. C. Location in Minnesota, USA.*

1072

## 1073 **S2. Methods**

1074

1075 Methods employed in water column analysis in BL are described in detail by Lambrecht  
1076 et al. 2018 and Lambrecht et al. in 2020. We review key approaches here.

1077

### 1078 *S2.1 Water column profiles*

1079

1080 Water column properties at BL were monitored using in situ sensors for dissolved  
1081 oxygen, temperature, conductivity, and pH with either a Hydrolab DS-5 sonde or a YSI  
1082 ProDSS. All sensors were calibrated according to the manufacturer's specifications.

1083  
1084     *S2.2. Water samples*  
1085  
1086     Water samples were collected from direct pumping for smaller samples, or a Van-Dorn  
1087     type opaque, non-metallic sampler for samples requiring larger volumes. Pumped  
1088     samples were collected from polypropylene or Tygon tubing, and immediately filtered in  
1089     the field with a filter connected to tubing to minimize exposure to O<sub>2</sub>. Samples for  
1090     cations, anions, and dissolved carbon (DIC, CH<sub>4</sub>) analysis were filtered at 0.45 µm.  
1091     Cation samples were preserved with HNO<sub>3</sub>, and CH<sub>4</sub> samples were preserved with HCl or  
1092     kept cool prior to analysis.

1093             Cations were analyzed by ICP-OES at the University of Minnesota Department of  
1094     Earth Sciences (2015 samples), or the U of MN Research Analytical Laboratory (2017-  
1095     2018 samples). Anions were analyzed at the same facilities using an ion chromatograph.  
1096     Samples for determining total sulfide were stored on ice or at 4°C until laboratory  
1097     analysis could be completed, usually within 72 hours, and analyzed by Cline assay  
1098     (detection limit: 1 µM; Cline, 1969; Reese et al., 2011) and measured  
1099     spectrophotometrically on an Epoch 2 Microplate Reader (Biotek). Nitrate and  
1100     ammonium samples were analyzed spectrophotometrically as described by Lambrecht et  
1101     al., 2018.

1102             Mineral saturation indices were calculated using Geochemist's Workbench  
1103     (Bethke, 1996) incorporating cation-anion data, DIC, and sonde measurements of O<sub>2</sub> (O<sub>2</sub>  
1104     measurements were entered as zero values below the detection limit of the sonde, usually  
1105     2-3 µM) and pH. Pseudokutnahorite saturation was calculated using Ca<sup>2+</sup>, Mn<sup>2+</sup>, and  
1106     CO<sub>3</sub><sup>2-</sup> activities calculated in Visual Minteq 3.1 (<https://vminteq.lwr.kth.se>) and the  
1107     solubility constant of Mucci (1991).

1108             Concentration of dissolved inorganic carbon (DIC) was determined by measuring  
1109     the CO<sub>2</sub> concentration of gas evolved from a 1 mL water sample injected with 1 mL of  
1110     85% phosphoric acid using a GasBench II system. The δ<sub>13</sub>C of DIC was measured from  
1111     the same evolved gas sample at the UC Davis Stable Isotope Facility (UCDSIF) a Delta  
1112     V Plus IRMS (Thermo Scientific, Bremen, Germany) coupled to the GasBench II. Final

1113  $\delta_{13}\text{C}$  values are expressed relative to the international standard V-PDB (Vienna PeeDee  
1114 Belemnite) with long term standard deviation of DIC analyses is 0.1 ‰.

1115 Stable isotope ratios of dissolved methane carbon ( $\delta_{13}\text{C}$ ) were measured at  
1116 UCDSIF using a ThermoScientific Precon concentration unit interfaced to a  
1117 ThermoScientific Delta V Plus isotope ratio mass spectrometer (ThermoScientific,  
1118 Bremen, Germany). Gas samples are scrubbed of  $\text{H}_2\text{O}$  /  $\text{CO}_2$  and  $\text{CH}_4$  is separated from  
1119 residual gases by a GS-CarbonPLOT GC column. Purified  $\text{CH}_4$  is oxidized to  $\text{CO}_2$  and  
1120 analyzed by IRMS. Standards are calibrated against NIST 8559, 8560, and 8561 and final  
1121  $\delta$ -values, are expressed relative to the international standards V-PDB (Vienna PeeDee  
1122 Belemnite) with long-term standard deviation of 0.2 ‰.

1123

1124 *S2.3. Particulates and sediments*

1125

1126 Water column particulate samples were collected in August 2018 by direct pumping of  
1127 BL water through Tygon tubing onto pre-weighed polycarbonate 0.2  $\mu\text{M}$  filters in  
1128 reusable polycarbonate housings from indicated depths until the filters became clogged.  
1129 Inlet and outlet hoses were then clamped to prevent oxygen contact, and collected  
1130 samples were immediately transferred into an  $\text{N}_2$ -filled glove bag for removal from the  
1131 filter housing and storage and transport in an  $\text{N}_2$ -filled airtight container with Oxoid™  
1132 AnaeroGen™ sachets (ThermoScientific).

1133 Surface sediment samples were also collected from BL in August 2018 using an  
1134 Aquatic Research Instruments gravity coring device. The top 1 cm of sediment was  
1135 extruded from the corer and immediately transferred to  $\text{N}_2$ -flushed 100 mL glass septum  
1136 bottles, stoppered with butyl rubber and crimped closed with aluminum caps.

1137 Water column sediment traps were deployed in BL from June through October  
1138 2018. Traps consisted of a 0.5-m polycarbonate tube of 2-inch diameter attached to a 1-L  
1139 Nalgene bottle. During recovery traps were immediately transferred into an  $\text{N}_2$ -filled  
1140 glove bag and trapped material transferred into large glass vials with butyl stoppers, and  
1141 subsequently stored in an anoxic glove box at Iowa State University.

1142 Filter particulates, sediment trap materials, and sediment samples were freeze-  
1143 dried. Mn was extracted from 50-100 mg of material using 10 mL of 0.5 M HCl for 1

1144 hour (Thamdrup et al., 1994). This extraction, used as part of the modified Fe sequential  
1145 extraction (Xiong et al., 2019) developed by Poulton and Canfield (2005), targets solid  
1146 phase Mn<sup>2+</sup>, and Mn carbonates, but only targets Mn-oxides if a reductant is present  
1147 (Thamdrup et al., 1994). Total Mn was determined following total digestion of the freeze-  
1148 dried samples by ashing at 550 °C followed by dissolution in HNO<sub>3</sub>-HF-HClO<sub>4</sub> and  
1149 evaporation to dryness. Boric acid was added to the residue (to dissolve aluminium  
1150 hexafluoride) and evaporated to dryness, before redissolution in 50% HCl. Mn in the  
1151 extractants were quantified by AAS (Thermo Scientific iCE3000 series) with RSD not  
1152 exceeding 2.1%.

1153

1154 *S2.4 X-ray diffraction*

1155

1156 Surface sample bulk mineralogy was assessed by powder X-ray diffraction. Samples  
1157 were gently homogenized in a cleaned agate mortar and loosely packed into an aluminum  
1158 target for analysis on a Rigaku Ultima-IV with Cu-K $\alpha$  radiation scanned from 5-75° 2 $\theta$   
1159 with a 0.02° step size with an X-ray energy of 44 kV and 40 mA. Counts were measured  
1160 with a D/Tex detector which allows for a scan speed of 6° per minute.

1161 The sediment trap sample, homogenized as above, was analyzed at Iowa State  
1162 University on a Siemens D500 diffractometer using Cu-K $\alpha$  radiation at 45kV and 30mA  
1163 from 4-75° 2 $\theta$  with a 0.05° step size and a scan rate of 2° per minute.

1164

1165 *S2.5 Geochemical modeling*

1166

1167 Brownie Lake cation, anion, DIC, pH, and O<sub>2</sub> data were imported to Geochemist's  
1168 Workbench (GWB; version 8.0.12 build 4427; Bethke, 1996) to assess the sensitivity of  
1169 carbonate mineral saturation to processes occurring near a ferruginous chemocline.  
1170 Activity coefficients were modeled utilizing the standard "B-dot" or extended Debye-  
1171 Huckel equation, which is valid in solutions with ionic strengths up to 3 molal (Bethke  
1172 and Yeakel, 2010); the maximum ionic strength of solutions we modeled was ~0.66  
1173 molal. Processes we considered included photoferrotrophy (as discussed in  
1174 Crowe et al., 2008), methanotrophy (Lambrecht et al., 2020), and sulfate reduction

1175 (Walter et al., 2014), in addition to processes that would be implicated in typical  
1176 temperate lake water columns including calcite dissolution and organic carbon respiration  
1177 (Myrbo and Shapley, 2006). To simplify our approach, we focused these efforts on three  
1178 primary carbonates: calcite, rhodochrosite, and siderite, though precursor metastable  
1179 carbonates likely play a role in these processes (e.g. Mucci, 1991; Jiang and Tosca, 2019;  
1180 Vuillemin et al., 2019). We also focus on calcite rather than aragonite as the former is the  
1181 primary phase in most freshwater lakes (e.g. Thompson et al., 1997), and recent  
1182 experiments demonstrate that the calcite lattice is more accommodating of Mn  
1183 incorporation than is aragonite (Son et al. 2019).

1184 To assess changes to mineral saturation and precipitation we ran scenarios in both  
1185 unsuppressed (minerals allowed to precipitate at saturation) and suppressed (mineral  
1186 precipitation blocked) conditions. Although the assumption that minerals would  
1187 precipitate at saturation is largely unrealistic (siderite in particular may require multi-fold  
1188 oversaturation, e.g. Jiang and Tosca, 2019; Vuillemin et al., 2019), this view of the  
1189 system is useful in assessing the ratios of minerals that could be produced by these  
1190 waters.

1191 In simulations where calcite was added, the rate of addition was tied to the  
1192 concentration of calcite that was generated in an unsuppressed simulation with Brownie  
1193 Lake surface water chemistry of July 2017 (surface water calcite abundance at  
1194 equilibrium 115.6  $\mu\text{mol}$  with dolomite minerals suppressed) and divided over the 15 day  
1195 simulation (7.7  $\mu\text{mol}$  calcite added per day). The length of the simulation was selected on  
1196 the basis of the duration of whiting events (days to weeks, e.g. Shinn et al., 1989;  
1197 Thompson et al., 1997) as well as seasonal changes observed between mid- and late  
1198 summer in the Brownie Lake water column manifested in the upward migration of the  
1199 oxycline (e.g. Lambrecht et al., 2018, discussion below). Simulations with longer  
1200 reaction times did not change the fundamental results, which were governed by initial  
1201 conditions and selection of reaction rates. These rates were determined based on dividing  
1202 initial concentrations of reactants measured in the water column (e.g.  $\text{O}_2$ ,  $\text{SO}_4$ ) by a 15-  
1203 day model simulation.

1204 An initial series of simulations assessed sensitivity of carbonate saturation to the  
1205 following processes: calcite addition,  $\text{CO}_2$  addition,  $\text{CO}_2$  removal, and sulfate reduction.

1206 Aerobic respiration (AR) and CH<sub>4</sub> oxidation (MO) were tracked using the following  
1207 stoichiometries:

1208



1210

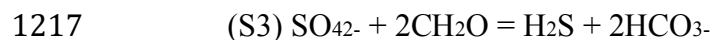


1212

1213 With the key differences being the ratio of O<sub>2</sub> removed to CO<sub>2</sub> added: 2:1 for MO, and  
1214 1:1 for AR.

1215 Sulfate reduction (SR) was simulated using the following stoichiometry:

1216



1218

1219 In all of the cases above the concentrations of CH<sub>4</sub> and CH<sub>2</sub>O were assumed to be  
1220 unlimited relative to the concentration of electron acceptors. The impacts of oxygenic  
1221 photosynthesis and photoferrotrophy were also assessed but found to have negligible  
1222 influence given the low light availability. The three intervals selected for detailed  
1223 modeling based on initial simulation each showed greater sensitivity to changes in Mn-  
1224 carbonate saturation relative to others.

1225

### 1226 **S3. Supplemental Results and Discussion**

1227

#### 1228 *S3.1 Phosphorus cycling in Brownie Lake*

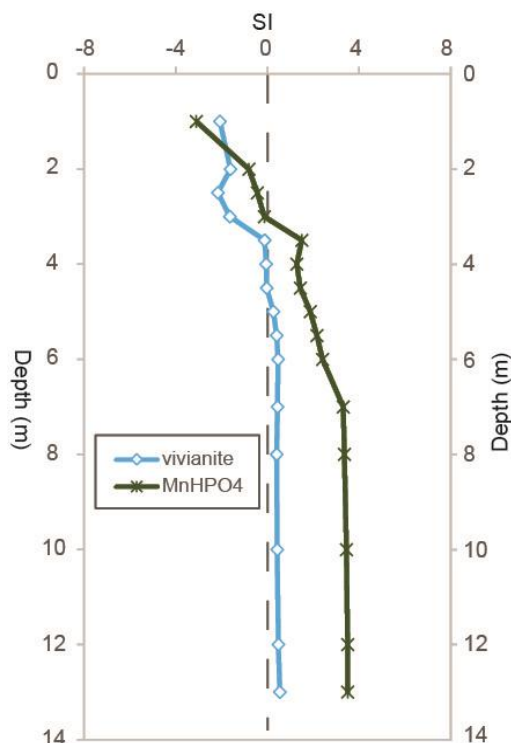
1229

1230 A Mn(II)HPO<sub>4</sub> phase becomes saturated at the chemocline, along with vivianite  
1231 (Fe<sub>2+3</sub>(PO<sub>4</sub>)<sub>2</sub>·8H<sub>2</sub>O; Figure S2). Both phosphate phases achieve maximum saturation in  
1232 deep water at 13 m depth (max SI = 0.54 for vivianite, max SI = 3.50 for MnHPO<sub>4</sub>). The  
1233 reliability of the solubility product of the Mn-PO<sub>4</sub> phase has been questioned (Schwab,  
1234 1989), hence we focus discussion in the main text on carbonate phases. However,  
1235 additional discussion of P-phases in ferruginous environments is warranted here.

1236 Phosphate phases are a significant particulate shuttle for Fe in ferruginous lakes  
1237 (Cosmidis et al., 2014), and may also play a role in the ferruginous Mn cycle.  
1238 Mn is recognized to substitute for Fe in diagenetic vivianite in both freshwater and  
1239 marine examples (Postma, 1981; Nakano, 1992; Friedl et al., 1997; Egger et al., 2015).  
1240 Vivianite and Mn-PO<sub>4</sub> phases are identified components in the particulate load from  
1241 ferruginous Lac Pavin (Cosmidis et al., 2014; Miot et al., 2016; Rivas-Lamelo et al.,  
1242 2017), with vivianite representing a dominant particulate component in deep waters.

1243 However, these phosphate phases are not detectable in surface sediment XRD  
1244 (main text). Vivianite may indeed be a component in BL sediments, but it does not  
1245 appear to play as large a role as calcite. Detailed assessments of phosphorus cycling in  
1246 Brownie Lake are the focus of ongoing work.

1247



1248

1249 Figure S2: Solubility index (SI) of phosphate phases in Brownie Lake, July 2017.

1250

1251

1252

1253

1254 *S3.2 Brownie Lake DIC mass balance analysis*

1255

1256 We employed a mass balance to determine the degree to which SR and MO may  
1257 contribute to the  $\delta_{13}\text{CDIC}$  excursion at the chemocline in BL. Using September 2017 data  
1258 (where the largest isotope excursion was observed), we consider the influence on DIC  
1259 composition from the equations S1-S3 above, which were rebalanced in terms of  
1260 bicarbonate:

1261

1262 (S4)  $\text{CH}_2\text{O} + \text{O}_2 = \text{HCO}_3^- + \text{H}^+$

1263

1264 (S5)  $\text{SO}_4^{2-} + 2\text{CH}_2\text{O} = 2\text{HCO}_3^- + \text{H}_2\text{S}$

1265

1266 (S6)  $\text{CH}_4 + 3/2\text{O}_2 = \text{HCO}_3^- + 3\text{H}^+$

1267

1268 Pathways S4 and S6 produce acidity, while pathway S5 leads to accumulation of  
1269 bicarbonate. Iron and manganese reduction may additionally contribute to methane and  
1270 organic carbon oxidation in this zone as discussed in 4.1 of the main text, but we will  
1271 focus the following discussion on these three pathways illustrated above as they are the  
1272 best constrained by presently available data.

1273 By assuming that the bulk of the  $\delta_{13}\text{CDIC}$  shift across the oxycline (from  $-9.88\text{\textperthousand}$  at  
1274 3 m to  $-11.98\text{\textperthousand}$  at 4 m) is attributable to aerobic respiration, we can evaluate the relative  
1275 influence of SR and MO on the remaining depletion to a minimum value of  $-12.87\text{\textperthousand}$   
1276 observed at 5 m. At this depth, 25  $\mu\text{M}$  of sulfide was measured, which would account for  
1277 an additional 50  $\mu\text{M}$  of bicarbonate at a  $\delta_{13}\text{C}$  of  $\sim-30\text{\textperthousand}$  (an estimate for the composition  
1278 of organic carbon, e.g. Havig et al. 2017). This would shift  $\delta_{13}\text{CDIC}$  to  $-12.32\text{\textperthousand}$ , or 0.5‰  
1279 higher than the observed value. Oxidizing an additional 29  $\mu\text{M}$  of methane (assuming a  
1280  $\delta_{13}\text{C}$  of  $-64\text{\textperthousand}$  for  $\text{CH}_4$ ) would shift DIC to the observed carbon isotopic composition, but  
1281 not its observed concentration. We account for the sharp increase in the concentration of  
1282 DIC at the chemocline by mixing with DIC at the  $\delta_{13}\text{C}$  composition of water at 5.5 m  
1283 depth ( $-11.85\text{\textperthousand}$ ), requiring 50  $\mu\text{M}$  of methane to be oxidized (in addition to sulfate  
1284 reduction) to counteract the influence of the large DIC concentration increase, or a total

1285 of 79  $\mu\text{M}$  of methane against 25  $\mu\text{M}$  of  $\text{SO}_4$ , or a ratio of ~3:1 MO:SR. Limiting MO to  
1286 only the cumulative concentration of dissolved  $\text{O}_2$  observed between 4-5 m (26.6  $\mu\text{M}$ ),  
1287 would oxidize 17.7  $\mu\text{M}$  of  $\text{CH}_4$ , which would shift  $\delta^{13}\text{C}$  to -12.43‰ against the total DIC  
1288 reservoir.

1289 These scenarios represent only a lower limit on the influence of SR and MO on  
1290  $\delta^{13}\text{CDIC}$  at the BL chemocline as we react only a residual amount of oxygen measured in  
1291 the water column: additional  $\text{CH}_4$  and  $\text{SO}_4$  could have reacted, and iron-sulfide burial in  
1292 particular may mask the true scale of SR in these waters.

1293

1294

1295

1296

1297

1298

1299

1300

1301

1302

1303

1304

1305

1306

1307

1308

1309

1310

1311

1312

1313

1314

1315

1316 *S3.3 Thermodynamic calculations*

1317

1318 Table S1 displays Gibbs Free Energy ( $\Delta G_{rxn}$ ) and redox potential of key reactions  
1319 discussed in the main text, as calculated from conditions measured in BL waters.

1320

Reaction	$\Delta G_{rxn}$ (kJ/mol)	E (V)
$CH_4 + 2 O_2 = HCO_3^- + H_+ + H_2O$	-815.2	-
$HS^- + 2 O_2 = SO_4^{2-} + H_+$	-764.8	-
$Fe^{2+} + 0.25 O_2 + 2.5 H_2O = Fe(OH)_3 + 2 H_+$	-64.99	-
$Mn^{2+} + 0.5 O_2 + H_2O = Pyrolusite + 2 H_+$	-51.65	-
Half-reaction		
$CH_4(aq) + 3 H_2O = HCO_3^- + 9 H_+ + 8 e^-$	-	0.202
$H_2S(aq) + 4 H_2O = SO_4^{2-} + 10 H_+ + 8 e^-$	-	0.290
$Fe^{2+} + 3 H_2O = Fe(OH)_3 + 3 H_+ + e^-$	-	1.060
$Mn^{2+} + 2 H_2O = Pyrolusite + 4 H_+ + 2 e^-$	-	1.228

1321

1322

1323 Table S1: Calculated  $\Delta G_{rxn}$  and E for key reactions discussed in text. All calculated based  
1324 on BL conditions in July 2017 6 m at temperature 7.6 °C (Table 1) except reactions  
1325 involving sulfide, which were calculated from September 2017 data at 5 m and a  
1326 temperature of 15.1 °C.

1327

1328

1329

1330

1331

1332

1333

1334

1335

1336 **Supplementary References**

1337

1338 Bethke, C., 1996. Geochemical reaction modeling: concepts and applications. Oxford UP, 397 p.

1339

1340 Bethke, C. M., and Yeakel, S., 2010. The Geochemist's Workbench Release 8.0 GWB Essentials

1341 Guide. RockWare, 122 p.

1342

1343 Busigny, V., Jezequel, D., Cosmidis, J., Viollier, E., Benzerara, K., Planavsky, N.J., Alberic, P.,

1344 Lebeau, O., Sarazin, G., and Michard, G., 2016. The iron wheel in Lac Pavin: Interaction with the

1345 phosphorous cycle. In: Sime-Ngano et al. (Eds.), Lake Pavin, Springer International, p. 205-220.

1346

1347 Cline, J. D., 1969. SPECTROPHOTOMETRIC DETERMINATION OF HYDROGEN

1348 SULFIDE IN NATURAL WATERS. Limnology and Oceanography, v. 14, p. 454–458.

1349

1350 Cosmidis, J., Benzerara, K., Morin, G., Busigny, V., Lebeau, O., Jezequel, D., Noel, V., Dublet,

1351 G., and Othmane, G., 2014, Biomineralization of iron phosphates in the water column of Lake

1352 Pavin (Massif Central, France): *Geochimica Cosmochimica Acta*, v. 126, p. 78-96.

1353

1354 Crowe, S.A., Jones, C., Katsev, S., Magen, C., O'Neil, A.H., Sturm, A., Canfield, D.E., Haffner,

1355 G.D., Mucci, A., Sundby, B., and Fowle, D.A., 2008. Photoferrotrophs thrive in Archean ocean

1356 analogue. *Proceedings of the National Academy of Sciences*, v. 105, p. 15938-15943.

1357

1358 Crowe, S., Katsev, S., Leslie, K., Sturm, A., Magen, C., Nomosatryo, S., Pack, M., Kessler, J.,

1359 Reeburgh, W., and Roberts, J., 2011, The methane cycle in ferruginous Lake Matano:

1360 *Geobiology*, v. 9, no. 1, p. 61-78.

1361

1362 Egger, M., Jilbert, T., Behrends, T., Rivard, C., and Slomp, C.P., 2015. Vivianite is a major sink

1363 for phosphorus in methanogenic coastal surface sediments. *Geochimica Cosmochimica Acta*, v.

1364 169, p. 217-235.

1365

1366 Friedl, G., Wehrli, B., and Manceau, A., 1997. Solid phases in the cycling of manganese in

1367 eutrophic lakes: New insights from EXAFS spectroscopy. *Geochimica Cosmochimica Acta*, v.

1368 61, p. 275-290.

1369

1370 Jiang, C.Z., and Tosca, N.J., 2019. Fe(II)-carbonate precipitation kinetics and the chemistry of  
1371 anoxic ferruginous seawater. *Earth and Planetary Science Letters*, v. 506, p. 231-242.

1372

1373 Lambrecht, N., Wittkop, C., Katsev, S., Fakhraee, M., and Swanner, E.D. Geochemical  
1374 characterization of two ferruginous meromictic lakes in the Upper Midwest, USA, 2018. *Journal*  
1375 of *Geophysical Research – Biogeosciences*, doi:10.1029/2018JG004587.

1376

1377 Lambrecht, N., Katsev, S., Wittkop, C., Hall, S.J., Sheik, C.S., Picard, A., Fakhraee, M., and  
1378 Swanner, E.D., 2020. Biogeochemical and physical controls on methane fluxes from two  
1379 ferruginous meromictic lakes. *Geobiology*, v. 18, p. 54-69, doi: 10.1111/gbi.12365.

1380

1381 Miot, J., Jezequel, D., Benzerara, K., Cordier, L., Rivas-Lamelo, S., Skouri-Panet, F., Ferard, C.,  
1382 Poinsot, M., and Dupart, E., 2016. Mineralogical diversity in Lake Pavin: Connections with water  
1383 column chemistry and biomineralization processes. *Minerals*, v. 6., doi:10.3390/min6020024.

1384

1385 Mucci, A., 1991. The solubility and free energy of formation of natural kutnahorite. *Canadian*  
1386 *Mineralogist*, v. 29., p. 113-121.

1387

1388 Myrbo, A., and Shapley, M., 2006, Seasonal water-column dynamics of dissolved inorganic  
1389 carbon stable isotopic compositions ( $\delta^{13}\text{C}_{\text{DIC}}$ ) in small hardwater lakes in Minnesota and  
1390 Montana: *Geochimica et Cosmochimica Acta*, v. 70, no. 11, p. 2699-2714.

1391

1392 Myrbo, A., Murphy, M., and Stanley, V., 2011. The Minneapolis Chain of Lakes by bicycle:  
1393 Glacial history, human modifications, and paleolimnology of an urban natural environment. In  
1394 Miller, J.D., Hudak, G.J., Wittkop, C., and McLaughlin, P.I., eds., *Archean to Anthropocene:*  
1395 *Field Guides to the Geology of the Mid-Continent of North America*, Geological Society of  
1396 America Field Guides 24, 425-437.

1397

1398 Nakano, S., 1992. Manganese vivianite in the bottom sediments of Lake Biwa, Japan.  
1399 *Mineralogical Journal*, v. 16, p. 96-107.

1400

1401 Novonty, E.V., Murphy, D., and Stefan, H.G., 2008. Increase of urban lake salinity by road  
1402 deicing salt. *Science of the Total Environment*, v. 406, p. 131-144.

1403

1404 Postma, D., 1981. Formation of siderite and vivianite and the pore-water composition of a recent

1405 bog sediment in Denmark. *Chemical Geology*, v. 31, p. 225-244.

1406

1407 Poulton, S.W., and Canfield, D.E., 2005. Development of a sequential extraction procedure for

1408 iron: implications for iron partitioning in continentally derived particulates. *Chemical Geology*, v.

1409 214, p. 209-221.

1410

1411 Reese, B.K., Finneran, D.W., Mills, H.J., Zhu, M.-X. and Morse, J. W., 2011. Examination and

1412 Refinement of the Determination of Aqueous Hydrogen Sulfide by the Methylene Blue Method.

1413 *Aquatic Geochemistry*, v. 17, p. 567–582.

1414

1415 Rivas-Lamelo, S., Benzerara, K., Lefevre, C.T., Montiel, C.L., Jezequel, D., Menguy, N.,

1416 Viollier, E., Guyot, F., Ferard, C., Poinsot, M., Skouri-Panet, F., Trcera, N., Miot, J., and Dupart,

1417 E., 2017. Magnetotactic bacteria as a new model for P sequestration in the ferruginous Lake

1418 Pavin. *Geochemical Perspectives Letters*, v. 5., doi:10.7185/geochemlet.1743.

1419

1420 Scholz, C., Talbot, M., Brown, E., and Lyons, R., 2011. Lithostratigraphy, physical properties

1421 and organic matter variability in Lake Malawi Drillcore sediments over the past 145,000 years:

1422 *Palaeogeography, Palaeoclimatology, Palaeoecology*, v. 303, no. 1, p. 38-50.

1423

1424 Schwab, A.P., 1991. Manganese-phosphate solubility relationships in an acid soil. *Soil Science*

1425 *Society of America Journal*, v. 53, p. 1654-1660.

1426

1427 Shinn, E.A., Steinen, R.P., Lidz, B.H., and Swart, P.K., 1989. Whitings, a sedimentologic

1428 dilemma. *Journal of Sedimentary Petrology*, v. 59, p. 147-161.

1429

1430 Son, S., Newton, A.G., Jo, K., Lee, J-Y., and Kwon, K.D., 2019. Manganese speciation in Mn-

1431 rich  $\text{CaCO}_3$ : A density functional theory study. *Geochimica et Cosmochimica Acta*, v. 248, p.

1432 231-241.

1433

1434 Swain, E.B., 1984, The paucity of blue-green algae in meromictic Brownie Lake: iron-limitation

1435 or heavy-metal toxicity [Ph.D. thesis]: Minneapolis, University of Minnesota, 362 p.

1436

1437 Thamdrup, B., Fossing, H., and Jørgensen, B.B., 1994. Manganese, iron and sulfur cycling in a  
1438 coastal marine sediment, Aarhus bay, Denmark. *Geochimica et Cosmochimica Acta*, v. 58, p.  
1439 5115-5129.

1440

1441 Thompson, J.B., Schultze-Lam, S., Beveridge, T.J., and Des Marais, D.J., 1997. Whiting events:  
1442 Biogenic origin due to the photosynthetic activity of cyanobacterial picoplankton. *Limnology and*  
1443 *Oceanography*, v. 42, p. 133-141.

1444

1445 Tracey, B., Lee, N., and Card, V., 1996. Sediment indicators of meromixis: comparison of  
1446 laminations, diatoms, and sediment chemistry in Brownie Lake, Minneapolis, USA. *Journal of*  
1447 *Paleolimnology* v. 15, p. 129-132.

1448

1449 Vuillemin, A., et al., 2019. Formation of diagenetic siderite in modern ferruginous sediments.  
1450 *Geology*, v. 47, p. 540-544.

1451

1452 Xiong, Y., Guilbaud, R., Peacock, C.L., Cox, R.P., Canfield, D.E., Krom, M.D., and Poulton,  
1453 S.W., 2019. Phosphorus cycling in Lake Cadagno, Switzerland: A low sulfate euxinic ocean  
1454 analogue. *Geochimica et Cosmochimica Acta*, v. 251, p. 116-135.

1455

1456 Walter, X.A., Picazo, A., Miracle, M.R., Vicente, E., Camacho, A., Aragno, M., and Zopfi, J.,  
1457 2014. Phototrophic Fe(II)-oxidation in the chemocline of a ferruginous meromictic lake. *Frontiers*  
1458 *in Microbiology*, doi: 10.3389/fmicb.2014.00713.

1459